Tampere University

Thomas Meric

CHRACTERIZATION OF GASB EDGE-EMITTING DEVICES IN 2 - 3 µM WAVELENGTH

Master of Science thesis
Tampere university
Supervisor: Nouman Zia
October 2021

ABSTRACT

Thomas Meric: Chracterization of GaSb edge-emitting devices in 2 - 3 µm wavelength
Master of Science thesis
Tampere University
Europhotonics programme
October 2021

This thesis is concerned with the theory, development and characterization of GaSb-based mid-IR mode-locked laser diodes (MLLD) and superluminescent light emitting diodes (SLED). MLLDs and SLEDs were grown by molecular beam epitaxy (MBE). The design process of the devices has been discussed. Deeply etched MLLD were tested for more than 5mW output power at about 2μm wavelength at room temperature under CW operation. A mode-locking operation was confirmed by spectrum measurement. The electrical resistance of the isolation section was found improved by the deep etching. 2.6μm wavelength SLEDs were tested for more than 31mW output power with 30$\%$ DC pump current at room temperature. The effectiveness of the cavity suppression design was confirmed by spectrum measurement. Instability of the beam profile for 2.6μm wavelength SLEDs was reported.

Keywords: Mode-Locked laser diode, superluminescent light emitting diode, edge-emitting laser diode, Quantum well, Gallium antimonide, III-V semiconductor, Infrared, Characterization of optical semiconductor components

The originality of this thesis has been checked using the Turnitin OriginalityCheck service.

PREFACE

This work has been realized in the optoelectronics research center (ORC) of the University of Tampere, in Finland.

I first want to thank my supervisor, Dr. Nouman Zia, for his supervision and his patience. I am grateful for his training in the experimental stages and for his clear explanations that helped me to better understand the topic of this thesis. Special thanks to Prof. Mircea Guinea for giving me the opportunity to do my Master's thesis there. I would also like to thank ORC's team for offering me such a good working environment. Great thanks to Dr. Topi Uusitalo for helping me when I needed it. I thank Ms. Maaret Hörkkö and Ms. Tea Vellamo for helping me with the bureaucracy.

I wish to thank the staff of the Europhotonics Master for offering me such great experiences. Big thanks to my students colleagues for their help and support during those 2 years.

I finally wish to thank my parents for their love and support during my long studies and my brother and sister for always pushing me to do my best. Je vous aimes!

Tampereella, 27th October 2021

Thomas Meric

CONTENTS

1. Intoduction 1
2. Theory 3
   - 2.1 Introduction 3
   - 2.2 Band structure and conditions for lasing 3
   - 2.3 Recombination Mechanisms in light-emitting devices 4
     - 2.3.1 Radiative recombination 4
     - 2.3.2 Non-radiative recombination 6
   - 2.4 Laser operation 7
     - 2.4.1 Threshold current 7
     - 2.4.2 Gain 8
     - 2.4.3 Cavity 9
   - 2.5 Temperature dependence 9
     - 2.5.1 Effect of heating on LD's characteristics 10
   - 2.6 Mode locking 11
     - 2.6.1 Active mode locking 11
     - 2.6.2 Passive mode locking 13
   - 2.7 Superluminescence 14
3. Design of laser diode 16
   - 3.1 Introduction 16
   - 3.2 Waveguiding 16
     - 3.2.1 Index guiding 16
     - 3.2.2 Gain guiding 19
   - 3.3 Far Field (FF) 19
   - 3.4 Mode-Locked laser diode (MLLD) design 20
   - 3.5 Superluminescent light emitting diode (SLED) design 21
4. Device fabrication 25
   - 4.1 Introduction 25
   - 4.2 Effect of strain on LD's characteristics 25
   - 4.3 Epitaxial structure 27
     - 4.3.1 GaSb substrate, buffer and cap 27
     - 4.3.2 InGaSb quantum wells (QW) 30
     - 4.3.3 AlGaAsSb cladding, separate confinement heterostructure and barrier 31
   - 4.4 Molecular beam epitaxy 32

4.5 Processing methods . . . 33
4.5.1 Plasma-enhanced chemical vapor deposition (PECVD) . . . 33
4.5.2 Reactive ion etching (RIE) . . . 34
4.5.3 Inductive coupled plasma reactive ion etching (ICP) . . . 34
4.5.4 Electron beam evaporation (E-beam evaporation) . . . 34
4.5.5 UV lithography . . . 35
4.6 Processing steps . . . 35
4.6.1 RWG etching . . . 35
4.6.2 Opening . . . 35
4.6.3 Metallization . . . 36
4.7 Last steps . . . 38
4.7.1 Thinning . . . 38
4.7.2 Dicing . . . 38
4.7.3 Mounting . . . 38
4.7.4 Wiring . . . 38
5. Results . . . 40
5.1 Introduction . . . 40
5.2 Devices studied in the analysis . . . 40
5.3 Characterization methods . . . 41
5.3.1 Optical power measurement. . . . 41
5.3.2 Far field beam profile . . . 42
5.3.3 Spectral measurement . . . 43
5.4 Characterization of 2μm wavelength mode-locked laser diode . . . 43
5.5 Characterization of superluminescent diode . . . 48
5.5.1 2.6μm wavelength emitting SLED . . . 48
5.5.2 2 μm wavelength emitting SLED . . . 49
6. Conclusion . . . 51
References . . . 52

LIST OF SYMBOLS AND ABBREVIATIONS

C	Auger coefficient
E_α	activation energy for auger recombination
R_{aug}	Auger recombination rate
Eg	Band gap
I	Current
N	Carrier density
L	Cavity length
q	Carrier charge
τ	Carrier lifetime
g_{dif}	Differential gain
β	Einstein coefficient for stimulated emission
n_e	Effective index
P_{sp}	Guided spontaneous power
v_g	Group velocity
g	Gain coefficient
P_j	Heating power
α_{int}	Internal losses
η_i	Internal quantum efficiency
a	Lattice constant
$\Delta\omega$	Longitudinal mode spacing
Γ_L	Lateral confinement factor
L_{gain}	Length of the gain section
L_{iso}	Length of the isolation section
L_{SA}	Length of the saturable absorber
A, B	Material parameters
α_m	Mirror losses
g_m	Modal gain=g Γ

D	Normalised thickness of active layer
W	Normalised width of active layer
P	Output power
Γ	optical confinement factor
N_p	Photon density
h	Plank constant
ν_p	Pulse repetition rate
ν	Photon frequency
τ_p	Pulse width
R	Reflectivity
n	Refractive index
G_s	Single pass optical gain
m_s	Spectral modulation
s	Strain
I_{th}	Threshold current
N_{tr}	Transparency carrier density
T	Temperature
d	Thickness of active layer
Γ_T	Transversal confinement factor
ω_m	Time varying loss frequency
V	Voltage
ko	Wavenumber in vacuum
k	Wave vector
λ	Wavelength
w	Width of active layer
AR	Anti-reflective coating
ASE	Amplified stimulated emission
AWG	Arbitrary wave form generator
CW	Continuous waveform
DC	Duty cycle
DE	Deep etched
EELD	Edge-emitting laser diode

fcc	Face-centred cubic
FF	Far field
FP	Fabry-Perot cavity
FWHM	Full width at half maximum
HH	Heavy hole
ICP	Inductive coupled plasma reactive ion etching
IR	Infrared (7μm to 1000μm)
LH	Light hole
LD	Laser diode
MBE	Molecular beam epitaxy
MLLD	Mode locked laser diode
OSA	Optical spectrum analyser
I-P-V characteristic	Plot of the optical power and voltage through the gain section in function of the injected current
PECVD	Plasma-enhanced chemical vapour deposition
QW	Quantum well
RHEED	Reflective high energy electron diffraction
RIE	Reactive ion etching
RWG	Ridge wave guide
SA	Saturable absorber
SCH	Separate confinement hetero-structure
SLED	Superluminescent light emitting diode
SO	Split-off
SRH	Shockley-Read-Hall non radiative recombination
TEC	Temperature electronic controller
UV	Ultraviolet (10nm to 400nm)
VCSEL	Verical cavity surface emitting laser

1. INTODUCTION

Light sources emitting in mid-infrared (IR)(2-3μm) have been increasingly interesting over the last years for many applications ranging from spectroscopic sensing to telecommunication [1, 2]. As a lot of molecules such as greenhouse gases (CO, CO2, N2O) or hazardous gases (NH3, HF) have a high absorbance at wavelengths around 2-3μm [3], mid-IR wavelength devices are particularly used for environmental control, industrial process monitoring and defense application [4]. Furthermore, those wavelengths are highly absorbed by water. Thus, making mid-IR wavelength devices eye-safe as human eyes are mainly composed of water. Mid-IR wavelength devices also show potential in telecommunication. Nowadays, most telecommunications devices are using near-IR wavelengths (1.3-1.55μm) [4]. To meet the continued steep growth in transmitted data volume, an interesting solution would be to use new spectral bands at longer wavelengths.

The main emphasis of this thesis is the development and characterization of compact, low-power consuming and efficient mid IR GaSb-based light emitting devices. Two device categories in particular were studied: 2μm wavelength mode-locked laser diodes (MLLD) and 2μm and 2.6μm wavelength superluminescent light emitting diodes (SLED). These devices are grown by molecular beam epitaxy (MBE), an epitaxial technique mainly used for its better control of the layer thicknesses and of the interface composition of the grown layers. A double quantum wells (QW) structure was chosen for the devices studied in this thesis in order to get a high output power and reduce the performance reduction due to the temperature. 2μm wavelength devices are using AlGaSb active layer while 2.6μm wavelength devices are using AlGaAsSb active layer. Two different waveguide geometries for MLLD were also investigated. GaSb-based mid-IR light emitting devices have several issues such as high rate of Auger recombination and free carrier absorption and high temperature sensitivity [5]. Despite those problems, many successful GaSb-based Mid-IR lasers have been grown [5].

MLLD are devices used to obtain ultrashort pulses (down to several fs) with high repetition frequency (up to Thz) [6]. There are other pulse generation techniques like gain switching or Q-switching but none of them can reach a pulse duration as short as with MLLD. The generation of ultrashort pulses is particularly useful for high resolution measurements of ultrafast processes like chemical reaction dynamics. MLLD emitting at 2μm wavelength are eye safe and thus are incredibly useful in LIDAR systems to measure velocity and

distance of object without wounding people [7]. In this thesis we studied a passive MLLD with a deeply etched ridge waveguide (RWG). This device was compared to an other passive MLLD with a more shallow waveguide geometry. Both devices have the same epitaxial structure and emit at the same wavelength. We also studied SLED devices with two different epitaxial structures, emitting at 2μm wavelength and 2.6μm wavelength respectively.

SLEDs are laser diodes (LD) with removed optical feedback mechanisms (either by using antireflective coating, RWG bending or both). This is done to prevent wavelength selectivity and spectral gain narrowing [8]. The resulting output beam combines the high power and beam directionality of LDs with the broad emission spectrum and low temporal coherence of light emitting diodes (LED), thus preventing interference patterns like speckles. Those properties make SLEDs particularly useful for optical coherence tomography, picoprojection or fiber optic gyroscopes [9, 10].

In chapter 2, we discuss the basic theoretical concepts required to understand this thesis. Chapter 3 present the designs of the devices studied. The emphasis will be on the waveguiding methods used for the RWG and the light emitting processes of the studied MLLDs and SLEDs. The epitaxial structure of those devices will be further discussed in chapter 4, along with the processing steps. The results will be presented in chapter 5. Finally, chapter 6 will summarize the most important results of this thesis and conclude with the future developments in this research topic.

2. THEORY

2.1 Introduction

In this chapter, we review the basic theoretical concepts required to understand this thesis. In section 2.2 we will present the band structure of semiconductor materials. In Section 2.3 we will discuss both radiative and non radiative mechanisms present in light emitting diodes. Some basic characteristics of laser operation will be presented in section 2.4. Finally, section 2.5 considers the effect of temperature on the performance of light emitting diodes.

2.2 Band structure and conditions for lasing

Electrons in semiconductor materials can only access specific energy states determined by Schrodinger's equation and quantum physics [11] . In semiconductors, those energy levels are very close to each other to the point we can approximate a package of possible energy states as a wide energy band [12]. The Fermi level defines the limit between bands fully occupied by electrons and the first empty band when the material is at a temperature of 0K [13]. The valence band is the highest occupied atomic energy band at 0K and the conduction band is the following higher-lying energy band. The valence band further consists of three sub-bands: heavy hole (HH), light hole (LH) and split-off (SO) valence bands. A representation of a semiconductor band structure is shown in Fig. 2.1.

Valence and conduction bands are separated from each other by a gap of inaccessible energy state called band gap Eg. In Fig. 2.1, the Semiconductor band structure is represented as the function of the crystal momentum associated to their electrons in the crystal lattice. The crystal momentum is represented by a wave vector k. A bandgap is called direct when the point with the lowest energy in the conduction band has the same wave vector k as the point with the highest energy in the valence band. On the other hand, when those two points are misaligned, it is called an indirect bandgap. The nature of the bandgap is defined by the material. The materials used in this thesis, like most III-V semiconductors, have a direct bandgap. Materials with a direct bandgap are particularly useful for light emission as they have a higher radiative recombination rate [15]. Light-emitting devices use recombinations of electrons from the conduction band

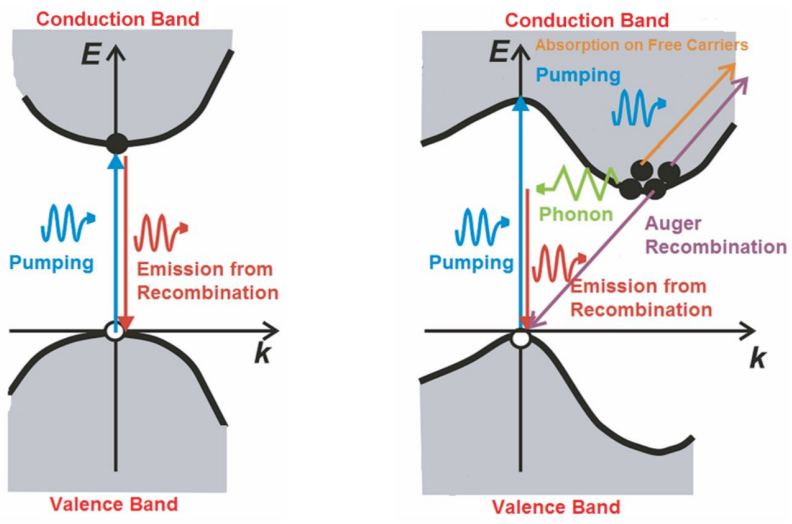

Figure 2.1. *Energy band diagram for semiconductors. Left: direct bandgap. Both valence and conduction bands are aligned. Left: indirect bandgap. The conduction band is misaligned with the valence bands [14]*

with holes of the valence band to produce photons with an energy equal to the bandgap [11]. Those recombinations can be classified into two categories: radiative recombination and non-radiative recombination (see Fig. 2.2).

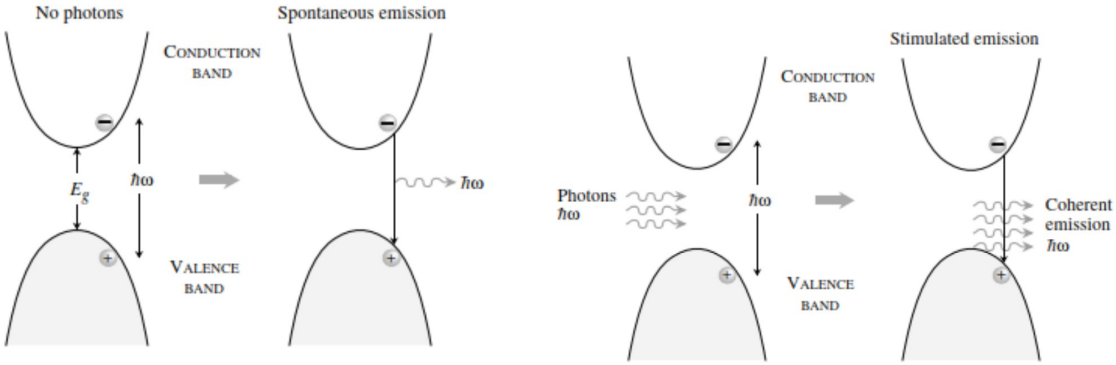

Figure 2.2. *Emission process [11]. Left: spontaneous emission. Right: stimulated emission*

Both radiative and non radiative recombination, along with their subdivisions, will be discussed in the next section.

2.3 Recombination Mechanisms in light-emitting devices

2.3.1 Radiative recombination

When an electron recombines with a hole, some energy is released in the form of photons. This is called radiative recombination. The frequency of a photon depends directly on its energy according to the Plank relation: E=hν with E the energy, h the Planck constant

and ν the frequency. Other parameters such as carrier density, confinement factor or temperature also affect the energy of the emitted photons. The two categories of radiative recombination are spontaneous emission and stimulated emissions [16].

spontaneous emission

Spontaneous emission is the most basic recombination. A photon in the conduction band moves spontaneously to the valence band by emitting a photon. The polarization and direction of emission of the photon are random. Spontaneous photons are incoherent. The rate of spontaneous emission can be increased by moving electrons from the valence band to the conduction band. This is done through pumping. A pump can be either optical by sending photons with energies larger than the bandgap or electrical by injecting carriers in the device.

Stimulated emission

In stimulated emission, the radiative recombination is caused by an incident photon. The generated photon has the same phase, direction and energy as the incident photon. Amplifying the rate of stimulated emission induces the emission of a high number of coherent photons. This is the basis of laser emission. As the probability for stimulated emission and photon absorption is the same, stimulated photons are susceptible to be reabsorbed almost immediately by electrons from the valence band. An inversion of population is required to enable the amplification of stimulated emission. Inversion of population is done by exciting electrons from the valence band to the conduction band. In this condition, there are almost no electrons in the valence band to absorb stimulated photons. When the number of stimulated emissions is larger than the number of absorption in the material, there is a net optical gain g.

Amplified spontaneous emission

Increasing the current of the injected pump has the effect of increasing the population inversion. As the conduction band is filled with electrons, the probability of spontaneous emission is increased. Photons that are produced by spontaneous emission induce new stimulated emissions that create a positive gain and amplify the optical power of the device. This is called amplified spontaneous emission (ASE) [17]. When the injected current reaches the threshold value, the number of electrons in the conduction band stops increasing. Stimulated emissions become more important than spontaneous emission and a lasing behavior appears instead of ASE. Some devices like superluminescent diodes (SLED) which avoid lasing (to get a wider spectrum for example) are inducing losses in their cavity in order to increase the threshold current and be able to increase further the rate of spontaneous emission through ASE.

2.3.2 Non-radiative recombination

There are several types of non-radiative recombination such as Shockley-Read-Hall (SRH) and Auger recombination that are reducing the performance of a device [13]. In semiconductor lasers emitting at longer wavelengths such as those we are studying in this thesis, Auger recombinations are predominant. Therefore, the other non-radiative recombination types will not be discussed. In the case of an Auger recombination, the energy lost by the de-excited electron moving from conduction to valence band is used to excite another electron from any energy band to a higher band. The high-energy electron eventually thermalizes back down to the bottom of the conduction band, inducing thermal vibration and increasing the temperature of the medium [12]. Auger recombination is separated into three different categories in function of the bands involved: CCCH, CHHS and CHHL. Fig. 2.3 represents the three different Auger recombination processes.

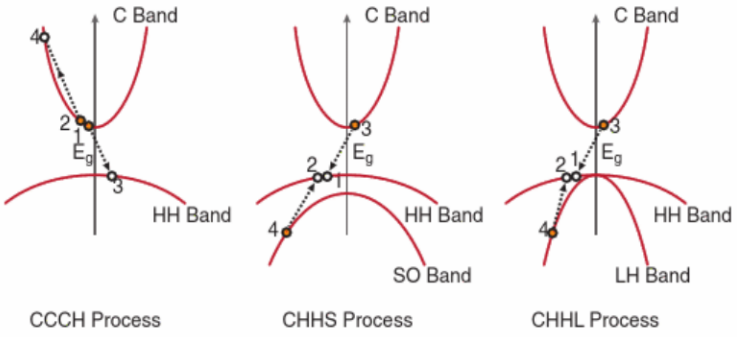

Figure 2.3. *Auger recombination processes [12]*

• CCCH: The energy of the first recombination is used to move an electron from the same conduction band to a higher band. The name CCCH comes from the bands involved in the process. Here, an electron moves from C to C (C for conduction band) and another moves from C to H (H for HH band)

• CHHS: The energy of the first recombination is used to move an electron from SO band to HH band, generating a hole in SO band.

• CHHL: The energy of the first recombination is used to move an electron from LH band to HH band, generating a hole in LH band.

Auger recombinations result from the collision between two electrons which knocks one electron down to the valence band and the other to a higher energy state. Therefore, Auger recombinations are more likely to happen when there is a high density of carriers inside the material. The Auger recombination rate is also increased when the bandgap is narrow as electrons can be moved to an upper band even with a small amount of energy. Temperature plays a major role too as a high temperature increases the agitation of the carriers inside the material, which increases the probability of collision. The temperature

dependence of Auger recombination is defined as [18]:

$$C_T = C_{300K} \exp\left(\frac{-E_a}{k}\right)\left(\frac{1}{T} - \frac{1}{300}\right) \tag{2.1}$$

With C the Auger coefficient, E_a the activation energy required to have an Auger recombination, T the temperature and k the Boltzmann constant. CHHS recombinations are negligible when the bandgap between the conduction and valence band is smaller than the gap between SO and HH band as all the energy is used for recombination that requires less activation energy like CCCH and CHHL [19]. That's why CCCH and CHHL recombinations are predominant in devices emitting in mid-IR. The rate of Auger recombination R_{aug} in laser is determined from the Auger coefficient as [20]:

$$R_{aug} = C * N^3 \tag{2.2}$$

with N the concentration of free electrons which is also equal to the concentration of free holes. Auger recombinations don't contribute to the light output of the device and therefore increase the current required to achieve an inversion of population and a lasing behavior. This increase is given by the formula [12]:

$$I_{NRth} = \frac{qVCN_{th}^3}{\eta_i} \exp\left(\frac{3(\alpha_m + \alpha_{int})}{g_m}\right) \tag{2.3}$$

With I_{NRth} the contribution of Auger recombination to the threshold current (I_{tot}=I_{th}+I_{NRth}), q the electric charge of the carriers, V the volume of the active region, N_{th} the carrier density at the threshold, C the Auger coefficient, η_i the internal quantum efficiency, α_m and α_{int} respectively the mirrors and internal losses and g_m the modal gain equal to the gain coefficient g multiplied by the optical confinement factor Γ.

2.4 Laser operation

2.4.1 Threshold current

It is important to empty and fill the valence and conduction band respectively to avoid reabsorption of photons emitted by stimulated recombination and to get a lasing behavior. By pumping the device (either with a photon flux or a current), electrons from the valence band are moved to the conduction band. In this thesis, we only work with electrically pumped laser diodes (LD). Compared to an optical pump, an electrical pump have a higher efficiency [21]. It is also possible to modulate the current (pulsed or continuous, pulse form and frequency, duty cycle, etc...). After a certain current called the threshold current Ith, the inversion of population is achieved. In other words, the optical gain in the

device is equal to the losses. The value of the threshold current is defined as [12]:

$$I_{th} = \frac{qVBN_{tr}^2}{\eta_i} \exp\left(\frac{2(\alpha_m + \alpha_{int})}{g_m}\right) \tag{2.4}$$

With I_{th} the threshold current, B the Einstein coefficient associated to stimulated emission and N_{tr} the transparency carrier density. Reducing the value of the threshold current is one way to improve a laser.

2.4.2 Gain

While propagating through the active region, photons trigger new stimulated emissions that amplify the total intensity of the light. The increase of optical power is represented by a value called optical gain g which is defined as [6]:

$$g = \delta(N_c - N_v) \tag{2.5}$$

with δ the absorption cross-section, N_c the carrier number in the conduction band and N_v the carrier number in the valence band. If the power saturation due to high temperature is neglected, the photon density N_p is amplified exponentially while propagating a distance z through the active region, according to the relation [12]:

$$N_p(z) = N_p(0) \exp^{gz} \tag{2.6}$$

The gain also connect the photon density to the carrier density N by the formula [12]:

$$\frac{dN}{dt} = \frac{n_i I}{qV} - \frac{N}{\tau} - v_g g N_p \tag{2.7}$$

With n_i the injection efficiency, I the injected current, v_g the group velocity, g the gain coefficient, q the charge of the carriers, V the volume of the active region and τ the carrier lifetime. Injecting more current increase the number of stimulated emission and so the gain of the device. However, after a certain value called saturated current, the gain saturates and power can decrease. This is the result of the rise of the temperature in the active region which increases the losses (see section 2.5.1). The saturated power P_{sat} is the maximum power achievable by a laser diode. Managing the temperature rise in the active region is a key step to improve the optical power of a device.

2.4.3 Cavity

Optical power can be amplified by placing the gain medium inside a cavity called Fabry-Perot(FB) cavity. Photons emitted in the gain medium by stimulated emission are reflected by the mirrors and pass through the gain medium several time, amplifying the light at each round trip. In most cases, one of the mirrors has a high reflectivity R (close to 1) and the other is semitransparent to get a light output. Both mirrors must have negligible absorption. A lasing operation is obtained when the modal gain of the gain medium is equal to the total losses of the cavity [22]:

$$g_m = \alpha_m + \alpha_{int} \tag{2.8}$$

with g_m the modal gain, α_m the mirror losses and α_{int} the losses due to the propagation through the gain medium. A FP cavity creates interferences between the propagating waves and the reflected ones. Only modes that have constructive interferences can effectively be amplified in a FB cavity. The wavelength of those modes, called resonant wavelengths, depends on the length of the cavity according to the formula [23]:

$$\nu = \frac{c}{2nL}m \tag{2.9}$$

which can be simplified as

$$\lambda = \frac{2nL}{m} \tag{2.10}$$

with ν the photon frequency, λ its wavelength, c the speed of light, n the effective index of the mode, L the length of the cavity and m an integer. Resonant modes that have a gain equal to their loss are called lasing modes and contribute to the optical output of the laser.

2.5 Temperature dependence

The operation of a laser produces heat in the active region. The rise of temperature can be attributed to several effects but the most important one is the Joule effect. Electrical pumping of a laser diode induces a flux of electrons through the laser. During their motion, some electrons transmit a part of their energy to the materials' lattices in the form of phonons that heat the material. This phenomenon is known as Joule heating, or ohmic heating. It is described by the Joule-Lenz law [24]:

$$Pj \propto V * I = R^2 * I \tag{2.11}$$

With Pj the heating power, I and V respectively the current and the voltage, and R the resistance of the LD. Joule heating is particularly effective in materials with a strong electrical resistance. One way to reduce Joule heating is to use a pulsed electrical pump rather than a continuous one. Under pulsed operation, the pulses are too short to effectively transmit heat to the device.

2.5.1 Effect of heating on LD's characteristics

Auger recombination

As seen previously, Auger coefficient is directly dependant on temperature [12]. Increasing the temperature also increases the rate of Auger recombinations which in turn increases the threshold current. Thus, it is important to keep a low temperature to have a device with the best efficiency. It is worth mentioning that Auger recombination also contributes to some extent to the heating of the device. After Auger recombination, the second excited electron return to lower energy band almost immediately. Instead of releasing photons, electrons diffuse thermic vibrations around them, leading to a rise in temperature in the medium.

Carrier leakage

A second consequence of high temperature is carrier leakage [25, 26]. At high temperatures, charge carriers have more energy. Some can have enough energy to cross the potential barrier at the edges of the QW and leak out of the active region. Such leakage reduces the efficiency of recombination as more charge carriers are required to achieve an inversion of population [27]. This results in a rise in the threshold current value and a reduction in the gain value. The variation of the threshold current Ith as a function of the temperature T is given by the formula [12]:

$$I_{th}(T) = I_{th}(T0)\exp(T/T0) \tag{2.12}$$

With $I_{th}(T0)$ the threshold current at the temperature $T0$. In addition to increasing the threshold current, the temperature is also responsible for the saturation of the LD's optical power. After a certain current value, the heating in the active layer becomes too important and reduces the gain to the point the optical power stop increasing and start reducing.

Bandgap shrinkage

A high temperature shrinks the bandgap between the conduction and valence band through lattice vibration. The relation between the bandgap Eg and the temperature T is given by

the empirical Varshni's law [28]:

$$E_g(T) = E_g(0) - \frac{AT^2}{B+T} \tag{2.13}$$

with A and B material parameters. The operation of the laser induces a rise in temperature around the active layer. The heat is mainly dissipated through the substrate because metals have a bigger thermal conductivity than air. Defining an epitaxial structure with the active region close to the submount is 1 way to reduce the deterioration of a device's properties due to temperature.

2.6 Mode locking

Mode-locked laser diode (MLLD) are devices that can emit high power pulses with ultra short pulse duration (on the order of femtoseconds) and high repetition frequency (on the order of terahertz) [7, 29, 30]. Two techniques are commonly used to achieve mode locking: active and passive mode locking.

2.6.1 Active mode locking

For active mode locking, a modulator creates either loss or refractive index variations through the devices in a periodic way. Those variations will modulate the amplitude of electric field of each cavity mode [6]:

$$E_l(t) = E_0[(1 - (\delta/2)(\cos(\omega_m t))] \cos(\omega_l t + \phi_l) \tag{2.14}$$

with $E_l(t)$ the electric field of mode l at time t, δ the depth of amplitude modulation, ω_m the frequency of the loss or refractive index modulation, ω_l the frequency of the mode and ϕ_l it phase. This equation can be written as [6]:

$$E_l(t) = E(t) + (E_0\delta/4)[\cos((\omega_m + \omega_l)t + \phi_l) + \cos((\omega_m - \omega_l)t + \phi_l)] \tag{2.15}$$

with

$$E(t) = E_0[1 - (\delta/2) - \cos(\omega_m t)] \cos(\omega_l t + \phi_l) \tag{2.16}$$

Thus, as seen in eq (2.15) the variation of refractive index or loss add two terms to E_l oscillating at the frequencies ω_l+ω_m and ω_l+ω_m, creating two modulation side-bands around the frequency of the mode ω_l (see fig. 2.4).

These side-bands can contribute to the electric field of the adjacent modes if the following

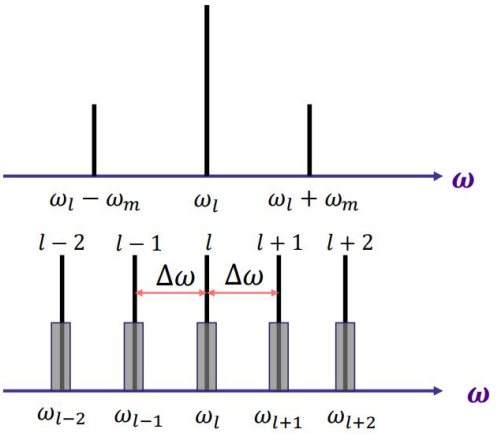

Figure 2.4. *The time-varying loss or refractive index creates two sidebands around the frequency of the mode [6]. When ω_m = $\Delta\omega$, each sideband overlap with the neighboring modes, coupling them together. In that case, phases are correlated such that ϕ_{l+1}- ϕ_l is constant. Thus, the phase of each mode is locked with respect to the adjacent modes.*

condition is met:

$$\omega_m = \Delta\omega \tag{2.17}$$

with $\Delta\omega$ the longitudinal mode spacing. If this condition is satisfied, the period of the modulation is equal to the cavity roundtrip time:

$$T = \tau_{rt} = 2L/c \tag{2.18}$$

with τ_{rt} the cavity roundtrip, L the length of the cavity and c the speed of light. Therefore, a pulse passing through the modulator when the loss is minimum will return to the modulator when the loss is once again minimum. On the other hand, a pulse slightly shifted from time of minimum loss will adjust itself back to the time of minimum loss as its wings will experience different losses, resulting in a shift of the pulse center (see Fig. 2.5) [6].

Eventually, every pulses are passing through the modulator when the loss is minimum, effectively locking the mode together. This results in the emission of ultrashort pulses with high repetition frequency and peak power. Active mode locking offers much more stability than its passive counterpart and generates pulses with less phase noises [4]. On the other hand, active mode locking can't produce pulses with picosecond pulse duration and has a limited repetition rate between two pulses. This is due to the active external modulation which is unable to achieve such high frequencies. Therefore, the MLLD devices studied in this thesis are all using passive mode locking.

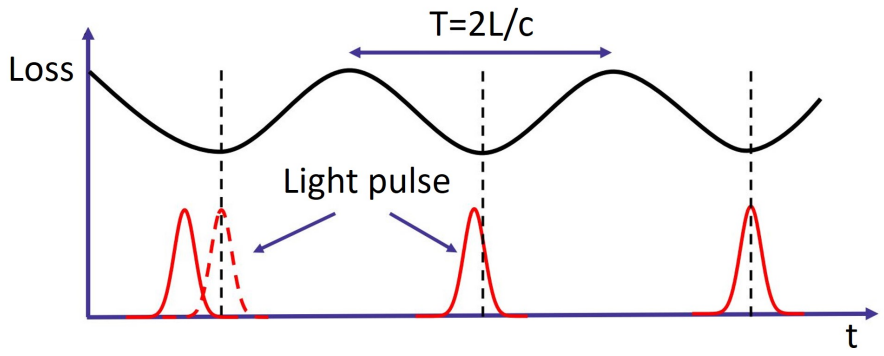

Figure 2.5. *Pulse shift due to loss variation. A misaligned pulse (solid line) will experience different losses on its leading edge and tail, gradually shifting the pulse toward the time of minimum loss where the pulse reaches a steady-state (in dashed line)*

2.6.2 Passive mode locking

Passive mode locking achieves mode locking by adding a nonlinear optical element called saturable absorber (SA) in the laser cavity. A schematic representation of the FP cavity of a passive MLLD is shown in Fig. 2.6.

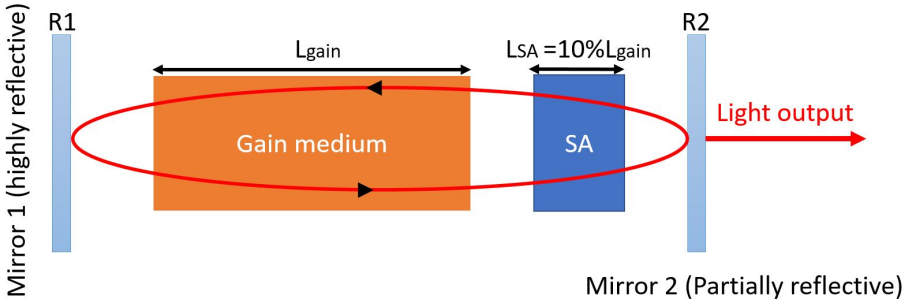

Figure 2.6. *schematic of FP cavity of passive MLLD device*

A SA introduces losses that are intensity dependant [6]. SA's absorption is very high when the intensity of the propagating mode is weak. On the other hand, losses are negligible for high intensity modes. When a high intensity pulses reach the SA, almost all the electrons from the valence band are excited to the conduction band. This depletes the valence band and fill the conduction band to the point where almost no other absorptions can occur, effectively reducing the losses for mode with high optical intensity. The cavity single pass power-loss when a SA is present can be written as [6]:

$$\gamma_t = \gamma - \gamma'(\frac{I}{I_s}) \tag{2.19}$$

with γ_t the cavity single pass power loss, γ the unsaturable single pass loss, γ' the low-

intensity single-pass loss of the saturable absorber, I the beam intensity in the cavity and I_s the absorber's saturation intensity. Since high powers are less attenuated by the SA, the peak power of a pulse will experience a higher roundtrip gain than its low power tail, eventually resulting in a shortening of the pulse. The shortening is limited by the relaxation time of the SA and by the gain bandwidth of the gain medium [6]. As the pulse duration decreases, its spectral bandwidth increases. When the spectral bandwidth exceeds the gain bandwidth, the wings of the pulse are not amplified anymore.

Since the loss of the SA is modulated by the propagating pulses themselves, this method can produce a higher repetition rate between pulses and shorter pulses than active mode locking [4]. The drawback of passive MLLD is a less stable pulse emission. It is possible to control the length of the emitted pulse by applying a reverse bias to the SA [31]. When a negative voltage is applied to the absorber, its relaxation time becomes shorter [4]. This leads to a shortening of the emitted pulses as it reduces the time window over which the losses are minimum [32]. Therefore, using a reverse bias is an efficient way to change the width of the emitted pulses at will.

2.7 Superluminescence

SLEDs are devices that combine a powerful spatially coherent beam like lasers and a low spectral coherence like LEDs [33]. SLEDs have an emission bandwidth bigger than LD while keeping the same beam quality. Those unique properties make SLEDs very useful for optical coherence tomography and pico-projector.

Superluminescence, also known as amplified spontaneous emission (ASE) is a light emitting mechanism that produces light with a powerful spatially coherent beam like lasers and a low spectral coherence like light emitting diodes (LED) [33].

The structure of superluminescent light emitting diodes (SLED) is pretty similar to standard LDs but the feedback of the FP cavity has been reduced to increase the threshold current. In LD, the number of spontaneous emissions stops increasing with the injected current when the threshold is reached and after the threshold, spectral gain narrowing can be observed in the device [8]. To avoid reaching the threshold, SLEDs have increased losses in the optical cavity which reduces the cavity feedback.

As seen in equation (2.4), the threshold current is dependent on the mirror losses. In order to increase the threshold current in SLED, it is possible to reduce the reflectivity of the facets in the optical cavity, which increases the mirror losses and so the threshold current. The condition to have a SLED operation is [33]:

$$\sqrt{R_1 R_2} = \frac{m_s}{2G_s} \tag{2.20}$$

with R_1 and R_2 the reflectivity of each facet, m_s the spectral modulation and G_s the single pass optical gain [34]:

$$G_s = \exp\left((\Gamma g - \alpha)L\right) >> 1 \tag{2.21}$$

with Γ the confinement factor, g the gain coefficient, α the single pass losses and L the length of the cavity. The condition presented in eq (3.12) is fulfilled if at least one of the facets has a reflectivity almost equal to 0. If both facets have low reflectivity, the device is called single pass. The output optical power of such device can be simplified as [34]:

$$P = P_{sp} G_s \tag{2.22}$$

with P the output power and P_{sp} the guided spontaneous power inside the cavity. If only one of the facets has low reflectivity, the device is called double pass. The light crosses the gain section two times instead of one, doubling the effective gain length [3]. Such devices focus all their optical power on the front facet that has low reflectivity, unlike single pass devices that emit light from both facets. Its output power can be simplified as [9]:

$$P = P_{sp} R_1 G_s^2 \tag{2.23}$$

with R_1 the reflectivity of the back facet. Double pass devices can reach higher power for lower injected current than single pass devices but they are also more susceptible to have a lasing behavior if the value of R_2 is not well set. Both single and double pass operations are represented in Fig. 2.7

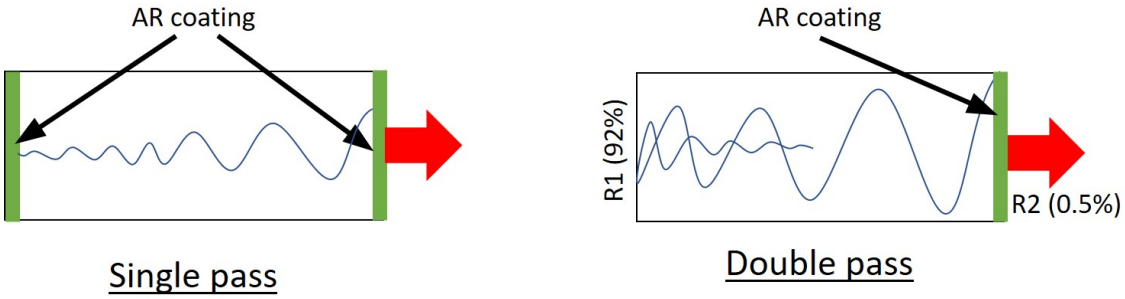

Figure 2.7. *Schematic presentation of amplified spontaneous emission in: (left) single pass and (right) double pass devices. In single pass device, both facets have low reflectivity whereas in double pass device the back facet has high reflectivity R1 which allows light to be reflected and lengthens the amplification path. Thus double pass devices have higher output power.*

3. DESIGN OF LASER DIODE

3.1 Introduction

The laser studied in this thesis includes MLLD emitting at about 2 μm wavelength and SLEDs emitting at about 2 μm and 2.6 μm wavelength. Devices emitting at the same wavelength are sharing the same epitaxial structure. The structure will be further discussed in section (4.3). MLLDs are devices exploiting stimulated emission and phase locking to create high power ultrashort pulses. On the other hand, SLEDs exploit amplified spontaneous emissions (ASE) to create a focused high power beam with low temporal coherence and high spectral width.

In section 3.2, we discuss the theory behind two kinds of waveguiding: gain guiding and index guiding. The far-field will be briefly discussed in section 3.3. Section 3.4 and 3.5 will present the design of the studied mode-locked laser diode and superluminescent light emitting diodes respectively.

3.2 Waveguiding

Edge-emitting light diodes (EELD) are generally comprising an active region and a resonator that provide optical feedback. The confinement of the mode in the active region, where the gain is maximum, is done by waveguiding techniques. The mode confinement in the vertical direction depends on the epitaxial structure of the device while the lateral confinement along the width of the device depends on the structure designed during the processing steps. In the following subsections, two main techniques used for lateral and vertical mode confinement are presented.

3.2.1 Index guiding

In index-guided devices, structural variations of refractive index are used to achieve wave confinement. An index guiding waveguide is made of a central confinement layer with a high refractive index n_2 surrounded by a cladding with a much lower refractive index n_1. By applying Snell's law (n_1 sin(θ1) = n_2 sin(θ2)), total reflection is achieved, effectively trapping the mode in the confinement layer [22]. In our devices, the active region act

as a confinement layer. The transversal confinement depends on the refractive index of the layers, the wavelength of the confined mode λ and the thickness of the active layer d. Transversal confinement of the mode is achieved if the following condition is satisfied [22]:

$$d < \frac{\lambda}{2}\sqrt{n_2^2 - n_1^2} \tag{3.1}$$

With d the thickness of the active layer, n_1 and n_2 the refractive indexes of the cladding and the active region respectively and λ the wavelength of the confined wave. In the same way, the wave can be confined laterally by having a much larger refractive index in the confinement region than the refractive index outside. A monomode can be successfully laterally confined if the following condition is satisfied:

$$w < \frac{\lambda}{\sqrt{8 n_e \Delta n_L}} \tag{3.2}$$

with w the lateral width of the active layer, n_e its effective index and Δn_L the lateral step index defined as:

$$\Delta n_L = n_2 - n_1 \tag{3.3}$$

The confinement is increased at higher step index values. The lateral confinement is achieved during the processing steps after the epitaxial growth. The most common way to get lateral confinement of the mode is to etch a ridge waveguide (RWG) on the device. A schematic of RWG is represented in Fig. 3.1 and the single-mode field is shown in Fig. 3.2

The width and depth of the RWG determine the number of modes propagating through the device. A wide RWG could confine several modes in the active layer and we would lose single mode operation. A multi-mode operation can also be observed for shallow RWG. There are several possible combinations of RWG width and depth that give a stable monomode operation. If the RWG depth is increased, its width should be reduced and vice versa. Both transversal and lateral confinement are characterized by a factor called confinement factor Γ. For fundamental mode, transversal confinement factor Γ_T and lateral confinement factor Γ_L can be approximated as [35, 36]:

$$\Gamma_T = \frac{D^2}{2 + D^2} \tag{3.4}$$

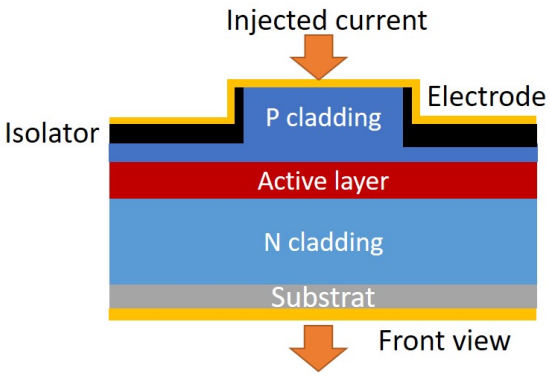

Figure 3.1. *Design of a RWG. The optical power is amplified in the active region. The claddings are used to confine the modes in the active region. They are p and n doped to facilitate the conduction of current through the device and the pumping. The isolator layer is used to force the injection of current through the top of the RWG. The pump current is injected through the top electrode. The substrate is the layer supporting all the structure.*

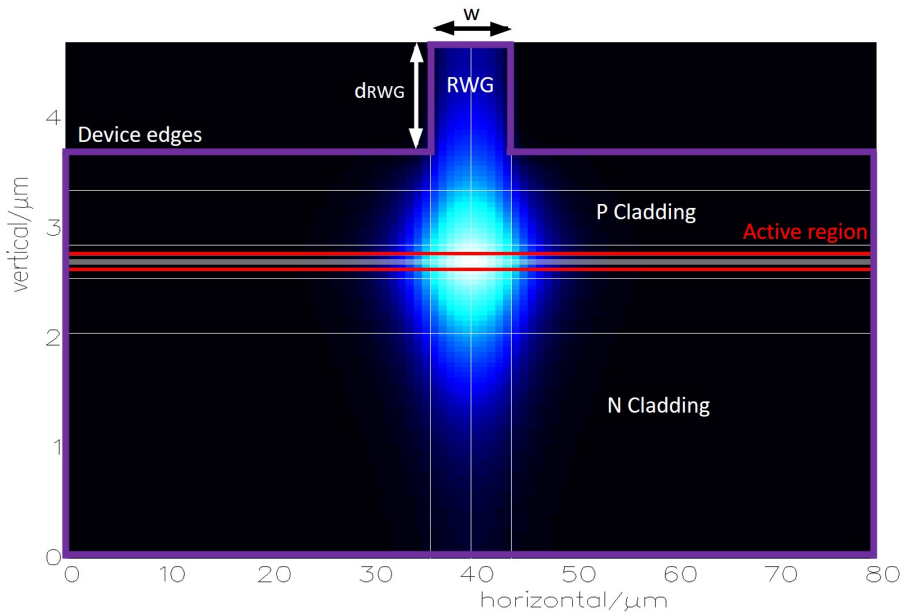

Figure 3.2. *Single-mode field in RWG device. The mode is successfully confined in the active region below the RWG.*

with D the normalized waveguide thickness:

$$D = ko\sqrt{n_2^2 - n_1^2} \tag{3.5}$$

ko being the wavenumber in vacuum. And:

$$\Gamma_L = \frac{W^2}{2 + W^2} \tag{3.6}$$

with W the normalized waveguide width:

$$W = w * ko * \sqrt{n_2^2 - n_1^2} \tag{3.7}$$

The total confinement factor is obtained by multiplying Γ_L with Γ_T [22]:

$$\Gamma = \Gamma_L * \Gamma_T \tag{3.8}$$

Index guiding is the guiding method that was chosen for the devices studied in this thesis.

3.2.2 Gain guiding

In gain guided devices, the wave is confined in the active regions due to high localized gain. The gain in the active region can be controlled by injecting charge carriers, according to the formula [12]:

$$g = g_{dif}(N - N_{tr}) \tag{3.9}$$

with g the gain, g_{dif} the differential gain, N the carrier density and N_{tr} the transparency carrier density. The optical mode stays confined in the active region where the gain is high. Gain guiding is pretty useful for lateral guiding as it does not require a RWG structure to effectively work. The vertical confinement is always done by index guiding due to epitaxial structure.

The main drawback of this method is that the injected current is not confined inside the active layer as it would be with a RWG [37]. Because of that, less of the injected current is used for the inversion of population, thus increasing the threshold current. Gain guiding is used most of the time for devices emitting at high power with multimodes.

3.3 Far Field (FF)

In edge-emitting laser diode, the small lateral and vertical dimensions of the active region diffract the field emitted from the laser waveguide. The non-diffracted field right at the output edge of the laser is called near field while the diffracted field some distance away is called far field. The shorter vertical dimension of the active layer creates a wider spreading of the beam along the axis, giving to the beam an elliptical cross-section. The axis perpendicular to the semiconductor layers is called fast axis while the axis parallel to the layers is called slow axis. It is most of the time desirable to have a stable beam shape as circular as possible and a Gaussian power distribution over the output field to facilitate the coupling with optical fibers and single mode waveguide.

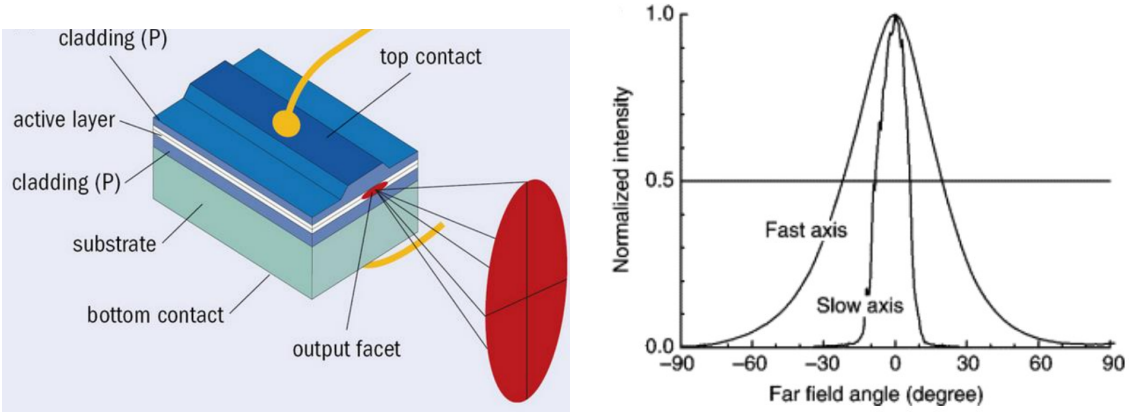

Figure 3.3. *Far field of edge-emitting device. Left: beam profile compared to laser structure. Right: Ideal power distribution over the beam profile*

3.4 Mode-Locked laser diode (MLLD) design

The MLLD studied in this thesis are passive mode-locked devices emitting at 2 μm wavelength. Those MLLD are made of two sections: the gain section which has a classical LD structure and the SA. Both sections are electrically isolated from each other by an isolation section as we are injecting a negative voltage to the SA and a positive current that induces a positive voltage to the gain section. If they were not isolated, the positive voltage in the gain section could reduce or even turn positive the voltage in the SA. The isolation is done by removing most of the p-layer on top of the RWG in the isolation section.

SA length is a major characteristic of the MLLD. If the absorber/gain length ratio is too small, the nonlinear effect induced by the SA will be too weak and a phase matching won't be achieved. On the other hand, if the ratio is too large, the absorption of the SA will be too strong and we won't get any light output [29]. The length for SA that was used in this thesis is about 10$\%$ of the total length of the FP cavity, similarly to other GaSb-based MLLD reported until now [30]. A schematic of MLLD design is presented in Fig. 3.4 (side, front and top view).

Deep etched (DE) MLLD design

As mentioned in the previous section, the electrical isolation between the SA and the gain section is essential to have a device with good performance. Unfortunately, there is always some leakage through the isolation section as the current can pass through the p-doped layer on the sides of the RWG. The current leakage has been simulated for different etch depths. The results are shown in Fig. 3.5.

Fig 3.5 shows that increasing the etch depth of the RWG is a good way to keep the current confined in the waveguide and to increase the electrical isolation between gain section

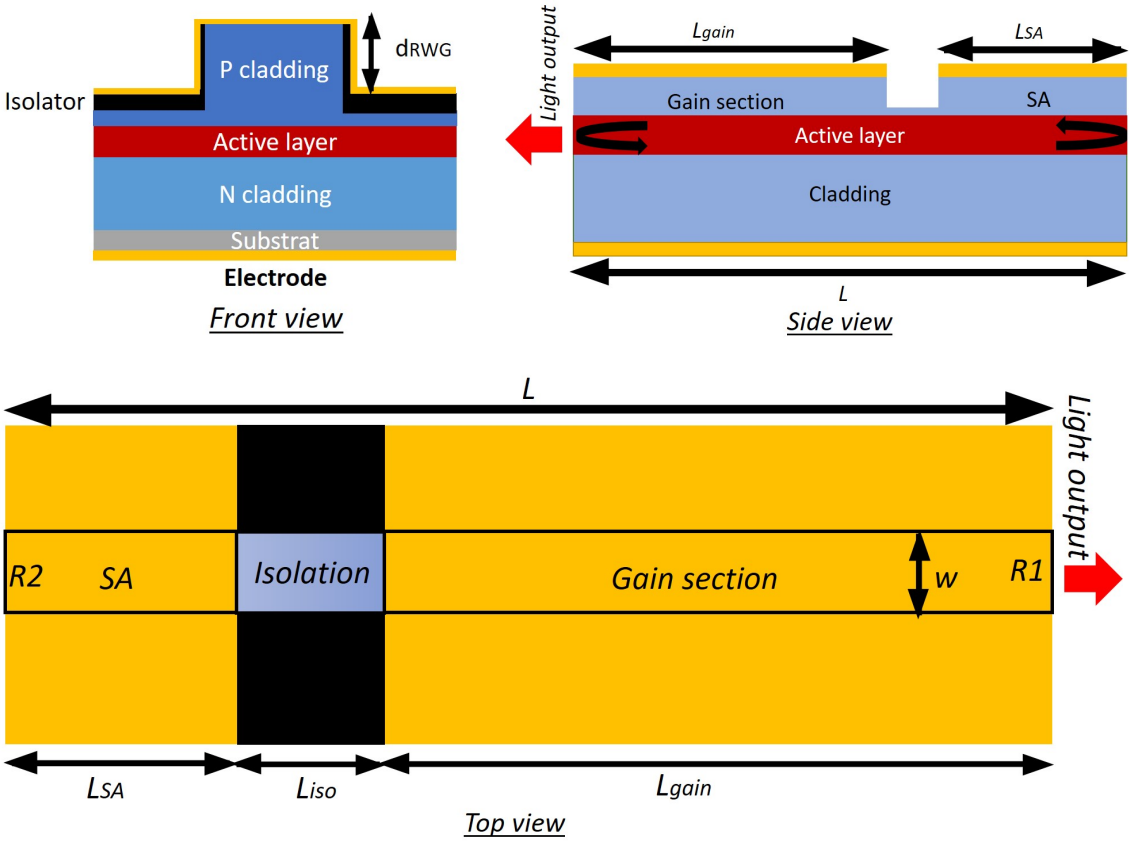

Figure 3.4. *Schematic of passive mode-locked device with important device parameters*

and saturable absorber [38]. In this thesis, we study a MLLD design created to increase the isolation between the gain section and the SA. The design is represented in Fig. 3.6.

This design is done by etching even more the trenches around the RWG. This prevents the current to pass by the sides of the RWG through the p-layer (see Fig. 3.6) and bypass the isolation [38]. Etching the sides of the RWG has two negative effects. Firstly, the deep etching creates defects along the sides of the RWG. Such defects create scattering that drastically increases the internal losses of the RWG [11]. Thus, the RWG is only etched over a limited length. Only the portion of the RWG in the isolation section is deeply etched. The other effect of etching is that it reduces the width of the RWG. The number of modes propagating in the RWG depends on its width and height (see section 3.2). Reducing the width of a monomode RWG causes the appearance of new modes. Increasing the depth of the waveguide is a good way to counterbalance the thinner width and stay in monomode.

3.5 Superluminescent light emitting diode (SLED) design

SLEDs are devices that combine a powerful spatially coherent beam like lasers and a low spectral coherence like LEDs [33]. SLEDs have an emission bandwidth bigger than LD

while keeping the same beam quality. Those unique properties make SLEDs very useful for optical coherence tomography and pico-projector. There are several ways to reduce the reflection of the facets.

• Anti-reflective (AR) coating (see Fig. 3.7.(a)): The reflectivity of the facets can be reduced by applying a coating made of a dielectric material [39]. AR coating is only effective for a specific wavelength which is a problem for SLEDs that have a broad range of emission wavelengths. It is still possible to use several AR coating to cover a broader range of wavelengths but it makes the fabrication process much more complex.

• Passive absorption (see Fig. 3.7.(b)): The reflectivity of the facets can also be reduced by putting a passive absorber before. The passive absorber can absorb the light before it reaches the facets, preventing any reflection [40]. However, the passive absorber can't reduce the reflectivity of the facets as much as AR coating. Even after absorption, there is still some reflection that contributes to the cavity feedback. Passive absorption was not used in this thesis either.

• Tilted Waveguide (see Fig. 3.7.(c)): When the axis of the cavity is not perpendicular to the facets, their reflectivity is greatly reduced due to destructive interferences [9]. the optimal tilting angle α to have minimal reflectivity depends on the width of the waveguide and its lateral step index. At optimal angle, the reflectivity of both facets can be reduced up to $10^{-}5$. Since the waveguide is tilted in front of both facets, tilted SLEDs are always single pass devices.

• Waveguide bending (see Fig. 3.7.(d)): Since double pass devices are more efficient than single pass devices, a bent waveguide was preferably used. The part of the waveguide near the output facet is tilted, effectively reducing its reflectivity [41]. However, the part of the waveguide near the other facet is kept straight. Such J-shaped waveguide turns the SLED into a double pass device. Waveguide bending is the method chosen for our devices. A schema of the SLED design is presented in Fig. 3.8

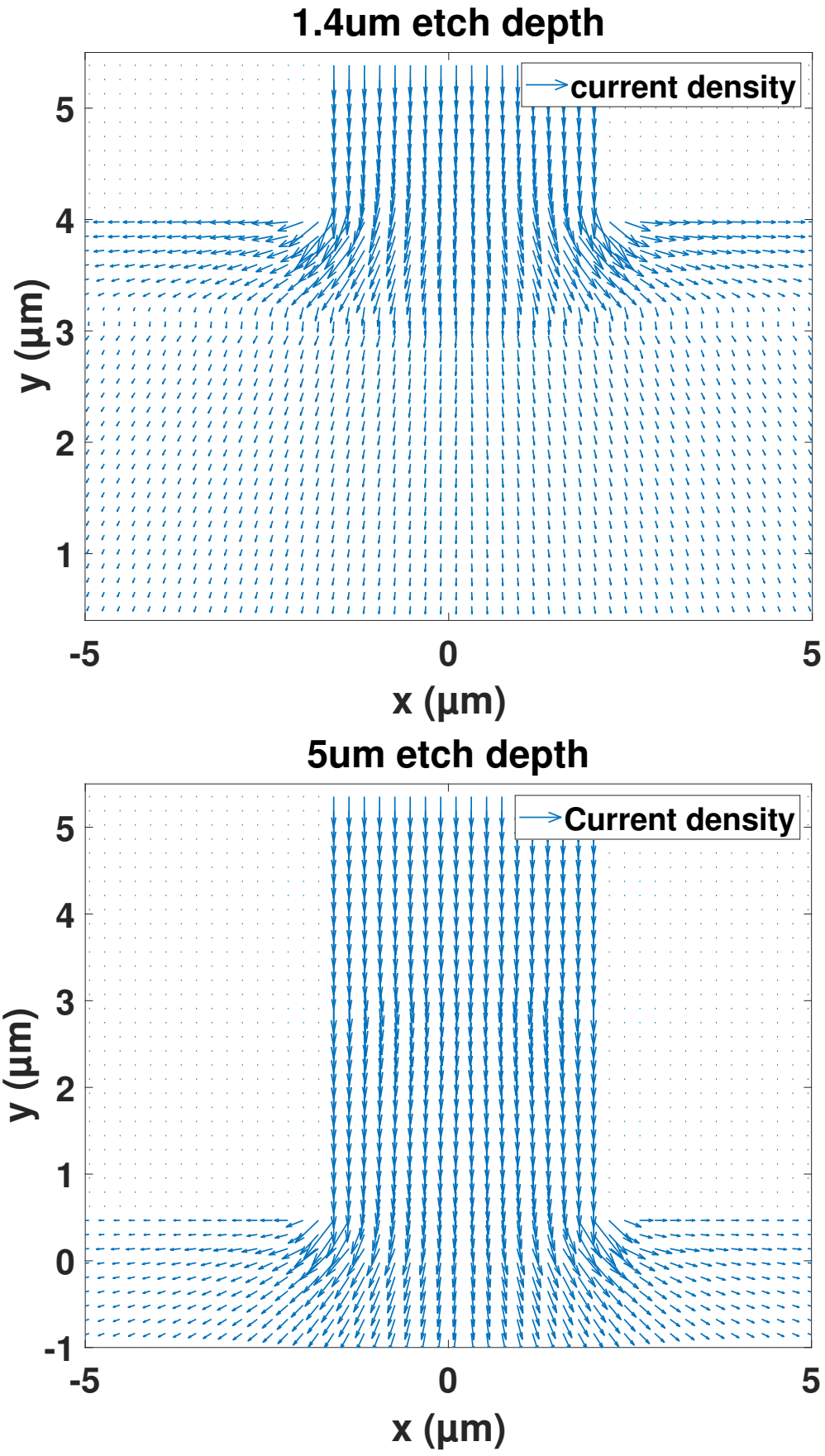

Figure 3.5. *Current density through the device. The current leakage on the sides of the central RWG is more important for shallow etch depth.*

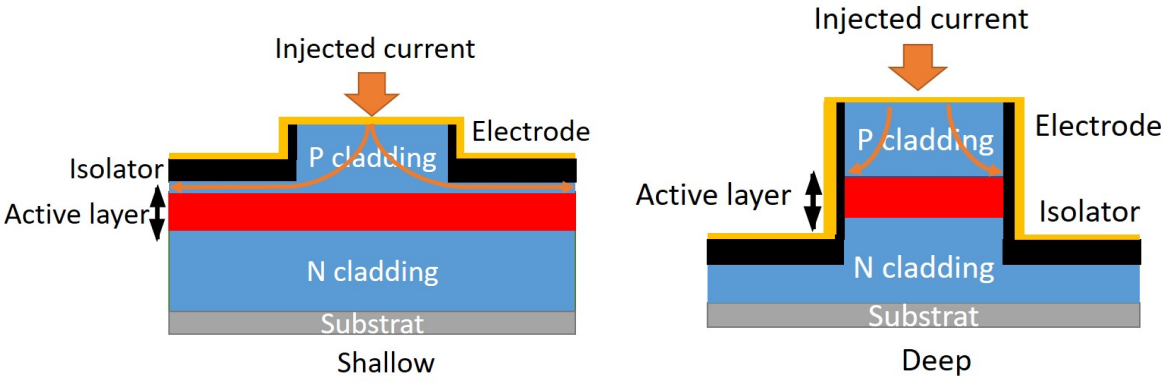

Figure 3.6. *DE design. Left: shallow RWG. The current can bypass the isolation section by going out of the RWG through the p-layer. Right: Deep etched RWG. By increasing the depth of the RWG, the current is no longer able to bypass the isolation section.*

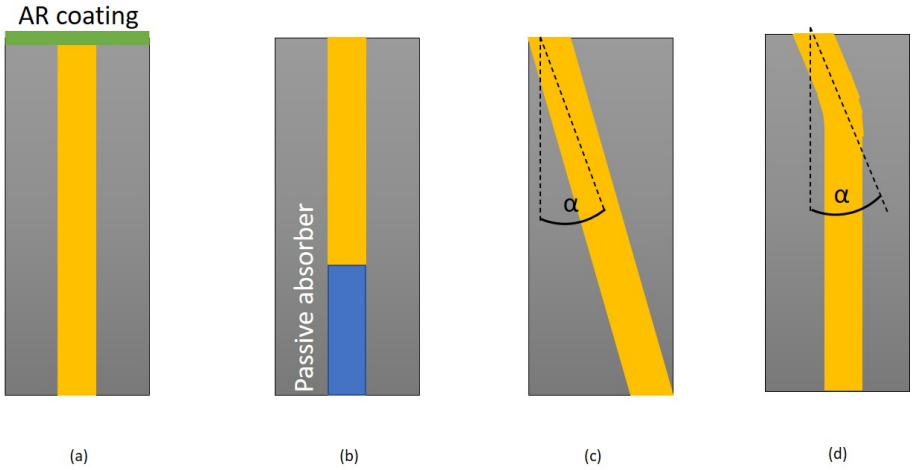

Figure 3.7. *Different SLEDs designs. (a) Anti-reflective coating. (b) Passive absorption. (c) Tilted waveguide. (d) Bent waveguide*

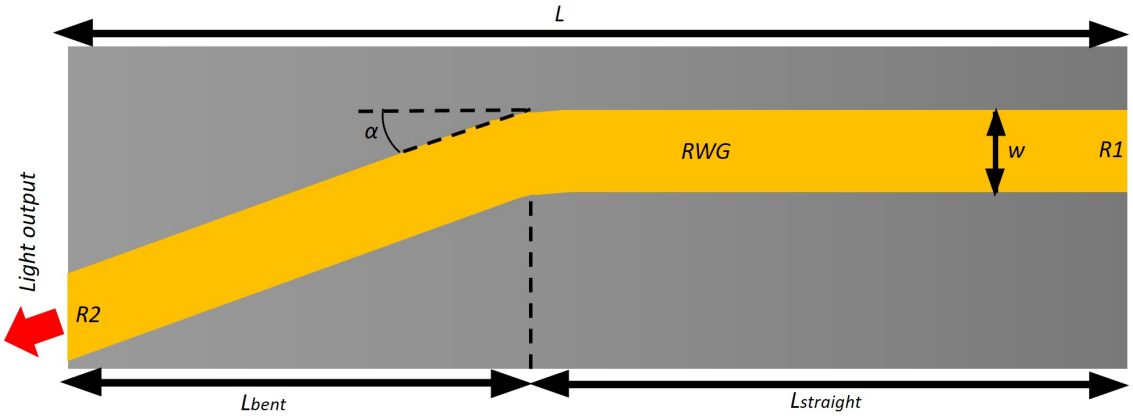

Figure 3.8. *2D schematic of SLED with important device parameters*

4. DEVICE FABRICATION

4.1 Introduction

In this chapter, we present the steps for laser fabrication. First, in section 4.2 we will explain the strains that can appear in the materials during the growth of the device and their effects. Section 4.3 will discuss the epitaxial structure of the studied devices. In section 4.4, we will present the epitaxial method used to grow the light emitting devices. Lastly, section 4.5 will explain the different processing methods used after the growth of the epitaxial structure.

4.2 Effect of strain on LD's characteristics

Semiconductors are materials with a periodic crystal structure. Their atoms are arranged in a basic pattern called unit cell that is repeated again and again through all the material. Most III-V semiconductor materials such as those used in this thesis have a face-centred cubic (fcc) unit cell with an extra atom at (x/4;y/4;z/4) from each of the atoms forming the corners of the cube (see Fig. 4.1).

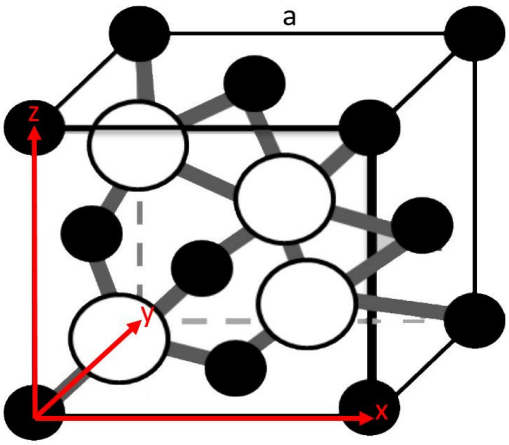

Figure 4.1. *Unit cell of GaSb*

x, y and z being the vectors of a Cartesian coordinated system with a magnitude equal to a, the length of the cube sides. Fcc crystal structure is defined by 8 atoms forming a cube whose sides have a length a and with an extra atom in the middle of each of the 6

faces of the cube. The length of the cube sides a is called the lattice constant of the unit cell. The lattice constant of an alloy can easily be calculated from the lattice constant of the materials that compose it with the Vegard's law [11]:

$$a_{(A_xB_y)} = x * a_A + y * a_B \tag{4.1}$$

with a_A and a_B being respectively the lattice constant of the material A and B and x, y their respective molar fraction in the alloy. The lattice constant is one of the most important parameters of crystals and plays a major role when growing a material on top of a substrate by epitaxy. In epitaxy, the grown material tries to match the lattice constant of the substrate [12]. Therefore, if the two materials have a different lattice constant, the crystal structure of the grown material will be distorted resulting in a tensile strain (if the substrate has a bigger lattice constant) or a compressive strain (if the substrate has a smaller lattice constant). Those distortions are represented in Fig. 4.2:

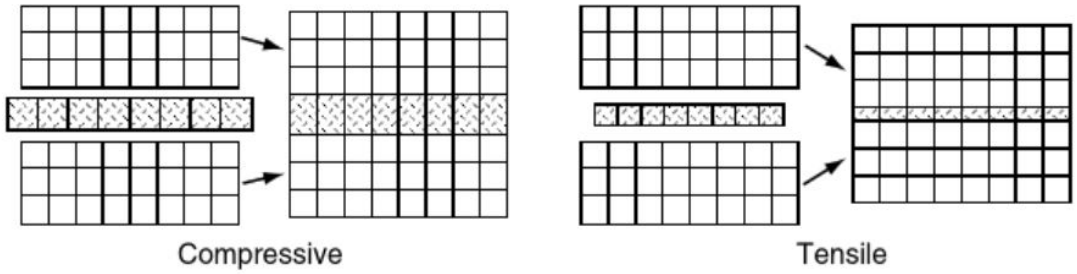

Figure 4.2. *Schematic of unit cell shape change due to strain if the lattice constant of the grown layer is different from the substrate lattice constant [12]*

The strain induced by the epitaxial growth of material on top of a substrate is given by the formula [11]:

$$s = \frac{a_s - a_L}{a_L} \tag{4.2}$$

with a_s the lattice constant of the substrate and a_L the lattice constant of the grown material. Stress is a source of defects such as oval defects, dislocation lines or point defects and affects the band structure of the materials [11]. Without stress, the light and heavy holes are distributed the same way in the valence band. Their energy bands are degenerated [42]. The stress induces an asymmetric change in the heavy and light hole distribution in the valence band (see Fig. 4.3).

HH and LH energy bands are no longer degenerated. Compressive and tensile strain respectively lower and lift the valence band of both HH and LH [42]. However, LH is much more affected by stress than HH and thus, LH moves above HH under tensile stress and below HH under compressive strain. When building a structure made of several materials,

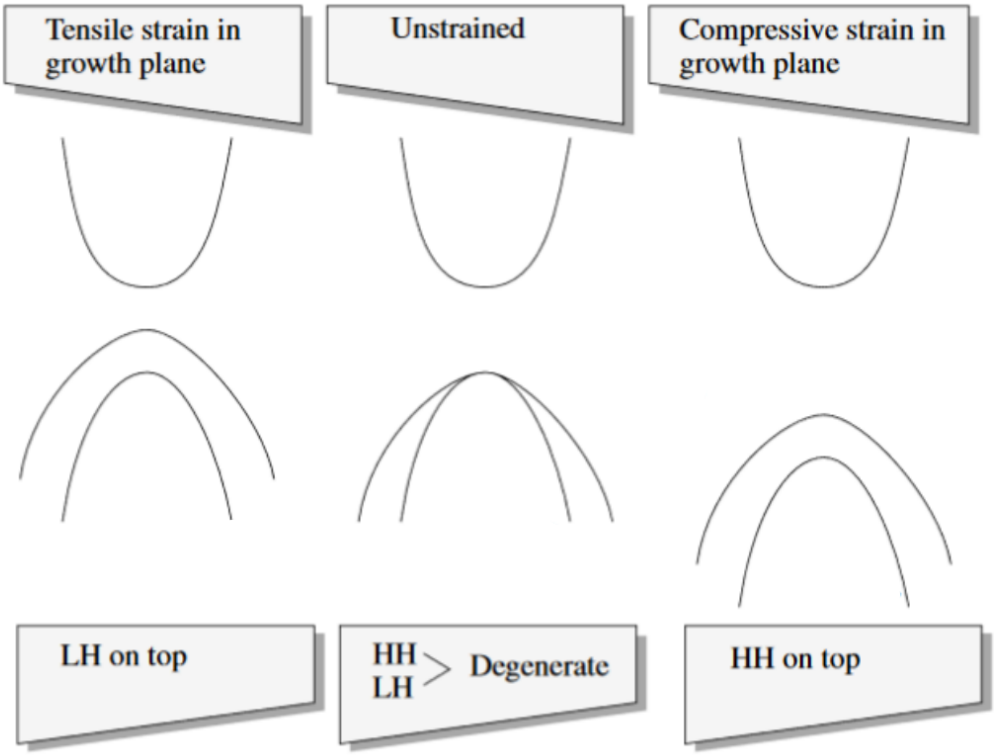

Figure 4.3. *Effect of strain over valence bands [11]*

it is important to consider the lattice matching in order to reduce strain and defects in the product. However, it can be useful sometimes to create strain in the material. To reduce Auger recombination by increasing the gap between light and heavy holes bands, for example [43].

4.3 Epitaxial structure

The epitaxial structure of a device defines its vertical confinement and its emission wavelength. In this study, devices emitting at (i) 2 μm and (ii) 2.6 μm wavelength were studied. This section will present the two structures associated with those emission wavelengths, the purpose of each layer and the materials used. Fig. 4.4 shows the band structure of 2 μm wavelength devices along with the vertical mode distribution.

Fig. 4.5 and Fig. 4.6 respectively summarise the epitaxial structure of 2 μm and 2.6 μm wavelength devices.

4.3.1 GaSb substrate, buffer and cap

The two structures studied in this thesis are GaSb-based. The substrate, cap and buffer of both structures are made of III-V gallium antimonide (GaSb) semiconductor. The substrate is the layer that supports all the structure of the device. But because it might get

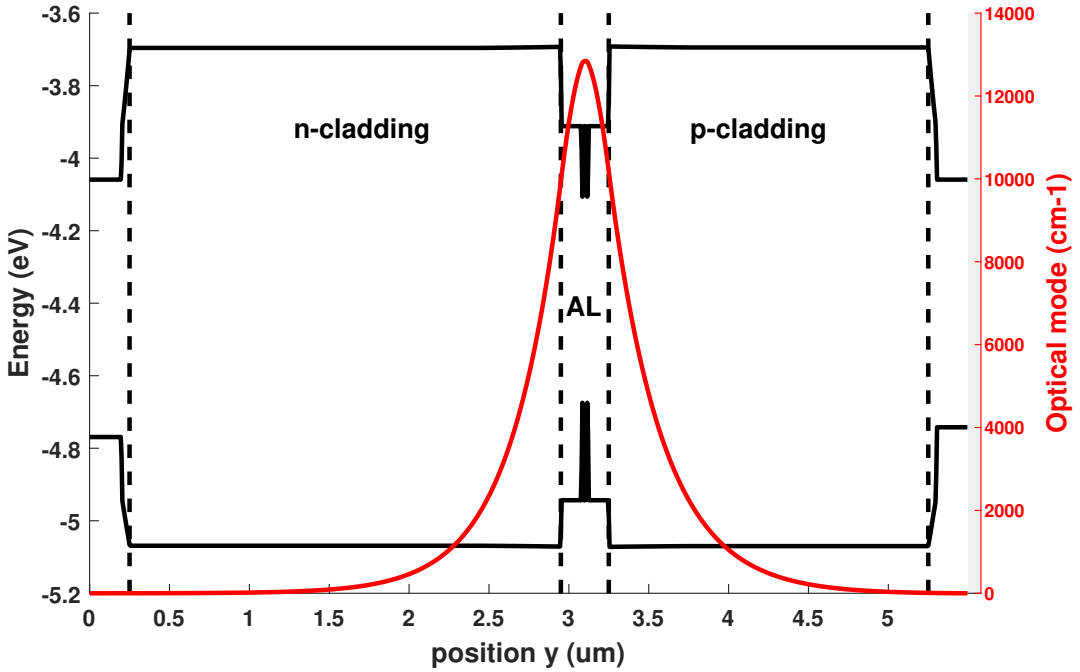

Figure 4.4. *Diagram of vertical mode distribution and band energy. The quantum wells are surrounded by separated confinement heterostructure (SCH) and form the active layer (AL). The cladding confines the charge carriers in the active region with its high bandgap that creates potential barriers while the optical mode is confined by the difference in refractive index between the cladding and the AL. The mode is maximum in the AL as it is the region where radiative recombinations take place. The mode decreases rapidly in the claddings and becomes neglectable after propagating 1 μm through it. This shows that the mode is well confined in the active region.*

Figure 4.5. *Epitaxial structure of 2 μm wavelength device*

damaged during its growth, a GaSb buffer was added to attenuate possible defects of the substrate and serves as a base free from defects for the rest of the structure. The top cladding of both structures contains aluminum and is therefore very sensitive to oxidation. A thin GaSb layer called a cap was grown on top of the structure to isolate the cladding from the oxygen in the air and prevent it from oxidizing. The cap layer is doped to not

Figure 4.6. *Epitaxial structure of 2.6 μm wavelength device*

create more ohmic resistance in the device. As mentioned in the previous section, the lattice constant a of an alloy can be calculated from the lattice constant of its components with Vegard's law. This empirical law only gives an approximation of the real value of the lattice constant of the alloy [44] but in our case, such precision is enough. Since GaSb is present in the other ternary and quaternary alloys used in the structures, its parameters are used to calculate the parameters of the alloys. When applied to a quaternary alloy, the Vegard's law is written as [28]:

$$a_{(A_xB_{1-x}C_yD_{1-y})} = (1-x)(1-y)*a_{BD}+x(1-y)*a_{AD}+y(1-x)*a_{BC}+xy*a_{AC} \quad (4.3)$$

The bandgap of the ternary alloys can also be calculated similarly but with the addition of a constant called bowing parameter C_{bow} [28]:

$$Eg_{(A_xB_{1-x}C)} = x * Eg_{AC} + (1-x) * Eg_{BC} - x(1-x) * C_{bow} \quad (4.4)$$

with x the molar fraction of group III elements A and B in the alloy and y the molar fraction of group V elements C and D. In our quaternary alloy $Al_xGa_{(1-x)}As_ySb_{(1-y)}$, the concentration of group III elements (Al and Ga) was set to get the desired bandgap while the concentration of group V elements (As and Sb) was set to get a phase matching with the other materials of the structure. The y molar fraction is obtained by solving Vegard's equation with the desired molar fraction for x [45]. The lattice constant a, bandgap Eg and refractive index n of the materials used in this thesis are presented in table 4.1.

Material	Eg(Ev)	a (Å)	n
$GaSb$	0.727	6.096	3.92
$Al_{0.5}GaAs_{0.04}Sb$	1.39	6.096	3.48
$Al_{0.3}GaAs_{0.04}Sb$	1.11	6.096	3.59
$In_{0.25}GaSb$	0.573	6.19	3.89

Table 4.1. *List of parameters of main alloys used in this thesis.*

4.3.2 InGaSb quantum wells (QW)

To increase the gain of a device, a QW is formed in the active region [46]. A QW is a potential well (meaning the materials around it have a higher conduction band and a lower valence band) with a thickness inferior to the De Broglie wavelength λ_b of the carriers [47]:

$$\lambda_b = \frac{h}{m * v} \tag{4.5}$$

with h the Planck constant, m the mass and v the velocity of the carriers. Typically, the width is between 5 and 20 nm wide. In QWs, electrons can access new sub-energy levels above the conduction band and below the valence band. As a result, the bandgap increases and the photons emitted have more energy (smaller wavelength) [48]. The value of the bandgap can be modified by changing the width of the QW, which changes the allowed energy level in it. The energy levels are quantified inside QW, unlike in the bulk material. This results in a reduction of the emission spectrum as fewer different band transitions are available. QWs are trapping charge carriers in the active region with high efficiency and therefore the inversion of population can be achieved with low pumping. The threshold current is greatly reduced and the extraction efficiency is increased. Quantum wells can be flooded, which limits the output power of the device. If the number of carriers in the QW is larger than the number of available states, the carriers might leak out and the recombination efficiency would be reduced. A similar problem also happens if the temperature of the electrons is too high. The electrons have too much energy and can escape from the QW, thus reducing its efficiency. A device with a single QW has a lower threshold current compared to multi QW structure. However, single QW structures have lower gain/output power [4]. Furthermore, they are more sensitive to variations of threshold due to temperature as single QW structures have a higher carrier concentration in the active region which increases the number of non radiative Auger recombination and the internal losses [43, 49]. To effectively confine the optical mode in the active region, QWs are required to have a refractive index much higher than their surrounding. This is mandatory to achieve index guiding (see section 3.2.1). We have chosen to use two

QWs for both structures to get a strong optical power. The 2 μm wavelength structure uses In(0.25)GaSb QWs. In(0.25)GaSb has a bandgap of 0.573 eV which is equal to an emission wavelength of about 2 μm (according to the formula E=h*c/λ) and is therefore a suitable choice for this structure. Increasing the molar fraction of indium reduces the bandgap and thus increases the emission wavelength of the QW [42]. Therefore, the extension of the emission wavelength up to 2.6 μm in the second structure was done by increasing the molar fraction of indium to 0.46. Doing so induces huge strains to the QW as In(0.46)GaSb lattice constant is much larger than GaSb lattice constant. An efficient solution is to use indium gallium arsenide antimonide (InGaAsSb) instead. The addition of arsenic significantly decreases the lattice constant of InGaSb [45]. Thus, arsenic is used to achieve lattice matching.

4.3.3 AlGaAsSb cladding, separate confinement heterostructure and barrier

The claddings are layers surrounding the active region whose purpose is to confine both optical modes and charge carriers in the QWs. As explained in section 3.2.1 and illustrated in Fig. 4.4, the mode confinement is achieved by using a cladding with a lower refractive index than the active region. On the other hand, the carrier confinement is achieved by using a material with a bandgap higher than the QWs as carriers from the QWs are required to have enough energy to pass through the potential barrier created by the energy gap between QWs and cladding bands to leak out of the active region. Both structures are using aluminum gallium arsenide antimonide (AlGaAsSb) for cladding as this material has the desired refractive index and bandgap. The main difference between the two structures is the Al composition. The 2 μm wavelength structure uses Al(0.5)GaAsSb while the 2.6 μm wavelength structure uses Al(0.6)GaAsSb. The composition of As and Sb was set to achieve lattice matching. The top and bottom cladding are respectively doped with holes (p-doping) and electrons (n-doping) to create a p-i-n junction. The doping values are the same for both structures and are presented in Fig. 4.5 and 4.6. Because of the doping, the rate of free carriers absorption is very high in the cladding [50]. To limit those absorptions that decrease the optical output of the device, a separate confinement heterostructure (SCH) was added between the cladding and the active region. SCH is not doped and uses the same material as the cladding, but with a different Al concentration: Al(0.3)GaAsSb for the 2 μm wavelength structure and Al(0.25)GaAsSb for the 2.6 μm wavelength structure. The SCH was also made much larger in the 2.6 μm wavelength structure with a width of 270nm instead of 130nm. SCH act as a buffer zone between the cladding and the active region where the optical mode can decrease without absorption [50]. When reaching the cladding, the optical mode is much weaker and thus the losses due to free carrier absorption are far less important. The two QWs are separated by a thin barrier layer that uses the same material as the SCH layer for both

structures. The barrier is used to separate the two QWs without reducing the intensity of the mode in the active region.

4.4 Molecular beam epitaxy

The epitaxial structure of our devices was grown using epitaxial method MBE. It was processed afterward with several methods in clean room. Lithography methods etch plane layers to give shape to the device. On the other hand, Epitaxy methods grow the crystalline structure of a layer by molecular deposition over a crystalline seed layer. This method shines for building plane layers and quantum objects like quantum wells and dots. The principle of epitaxy growth is to send reactants on the surface of a crystal seed. The transport of reactants can be done using gas flux, molecular beam or other methods depending on the epitaxial method used. After reaching the surface, the reactants are adsorbed and diffuse to an “equilibrium” position where they are incorporated into the layer (some atoms may desorp back to vapor). The grown layer tries to match the crystal structure and the lattice constant of the crystal seed. A difference of lattice constant between the two creates either a tensile or compressive strain. Strains have a huge impact on the performance of a structure. The main advantage of this method is that it’s easy to prevent any impurities in the final product. The growth process can also be changed at any time.

Molecular beam epitaxy (MBE) is the main epitaxial method used to build the devices used in this thesis [51]. MBE is an epitaxial method that works very well to grow III-V semiconductor compounds. Its specificities compared to other epitaxy methods are the growth at high temperature (around 600-700 C) in ultra-high vacuum and the use of Knudsen cells to project molecules on a wafer as a molecular beam. The high temperature is used to remove impurities and oxide from the wafer. It also increases the adsorption rate and the surface mobility of the atoms, allowing them to move easily on the wafer and speeding up the growth rate. On the other hand, the Ultra High Vacuum is used to prevent the appearance of impurities on the final product (unwanted particles in the growth chamber could be adsorbed by the substrate) and to be sure that the molecular beam interacts only on the wafer surface and not with the particles on its way. An MBE device is mainly made of two parts: a preparation chamber and a growth chamber. A schematic of the growth chamber is represented in Fig. 4.7:

First, the wafers are put inside the preparation chamber. There, they are heated to be outgassed. This is an essential step to achieve the required ultra-high vacuum. The gas in the wafer is released under high temperatures. Therefore, the wafer is heated before the growth in order to release all the gases and avoid any outgassing inside the growth chamber with ultra-high vacuum. After being prepared, the wafers are moved inside the growth chamber and exposed to the molecular beam from Knudsen cells (or Effusion

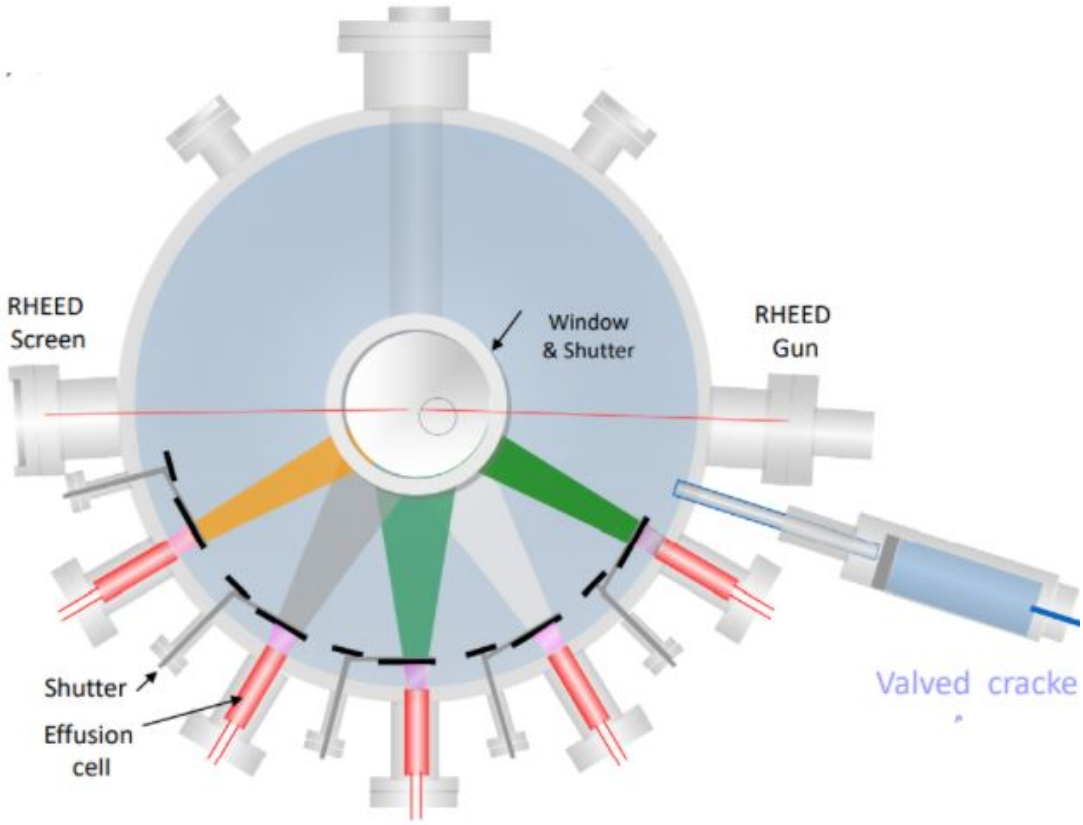

Figure 4.7. *Schematic of growth chamber*

cells). In each cell are put high quality ingots of the materials we want to grow. The role of those cells is to evaporate the ingots and to project them on the wafer as a molecular beam. Once the atoms reach the wafer, they condensate and are adsorbed by the wafer. Once adsorbed, atoms can move along the surface before getting adsorbed on favorable locations such as step edges or nucleated islands. This step is improved by the high temperature of the wafers. It is worth noting that while the inside of the growth chamber is very hot, its walls are cooled by liquid nitrogen. This is done to condensate on the walls any stray atom that would perturb the ultra high vacuum in the chamber. The growth is controlled by various means such as Reflective High Energy Electron Diffraction (RHEED) system.

4.5 Processing methods

4.5.1 Plasma-enhanced chemical vapor deposition (PECVD)

PECVD is a method used to grow thin films made with dielectric materials [52]. The wafer is placed between two electrodes. The lower electrode is connected to a radio frequency generator while the upper electrode is connected to the ground. The RF generator set a

rapidly oscillating electric field between the two electrodes. The desired dielectric material for the film is introduced between those two electrodes as a gas. The gas is then turned into plasma by the electric field. This plasma contains reactive radicals that can easily stick to the surface of the wafer, growing the thin film. In our study, PECVD was used to grow SiO2 and SiN films.

4.5.2 Reactive ion etching (RIE)

RIE is pretty similar to PECVD in its principle. They both share the same 2-electrodes structure with an RF generator creating a plasma between the two. The difference is that in RIE, the ground electrode is connected to a capacitor that absorbs electrons from the plasma [53]. Because of that, we end up with a plasma made of positive and heavy protons. Those protons are bombarded on the surface by the voltage created by the RF generator. The choice of the gas used for RIE depends on the material we want to etch. In this thesis, RIE is used to etch the SiO2 film that was grown with PECVD and the gas used for the etching was a mix of Argon and carbon hydro-trifluoride (CHF_3). The first one is used for the actual etching while the second is used to remove the non-volatile debris of the etching.

4.5.3 Inductive coupled plasma reactive ion etching (ICP)

ICP works with the same principle as RIE but uses two generators to separately control the generation of plasma and the bombarding rate [54]. ICP is particularly useful to reach denser plasma without increasing protons bombarding. ICP was used to etch GaSb-based layers in order to create the RWG. Since it's crucial to create a RWG with the correct dimensions, several etching times are performed on test samples to be sure to have exactly the good RWG depth. The gases used are nitrogen N_2 to protect the side walls from lateral etching (passivation) and Chlorine Cl_2 to prevent the etching rate of the QWs that contains indium and do not damage this layer.

4.5.4 Electron beam evaporation (E-beam evaporation)

To successfully inject electric current through the device, the top surface of the RWG must be covered by a metallic material. This is done by E-beam evaporation. Electrons are accelerated by applying a strong voltage of about 10 kV and sent on the metal we want to apply [54]. The shock of the electrons is strong enough to evaporate the metal. The metallic vapor is then condensed on the surface of the device, forming a thin film. Three different metals were used in our device. First, an extremely thin layer (about 30nm thick) of titanium is evaporated. This titanium layer serves to improve the adhesion of the particles of the other metals. The second layer is made of platinum. This one

is twice thicker than the titanium layer. It serves as a barrier to separate metals and semiconductors. The last layer is made of gold, a metal very well known for its good conductivity and its resistance against oxidation. That layer is twice thicker than the layer of platinum. Since the sides of the RWG must also be metallized and not just the top and bottom of the device, the laser is slightly tilted during the metallization.

4.5.5 UV lithography

The use of photoresist play a major role in the processing steps. During etching, the photoresist act as a protection to keep some areas unetched. Photoresist is spread on top of the semiconductor by spinning the device at high speed [54]. The photoresist is then exposed to UV light which activates a photoactive compound present in the resist. The activated photoresist becomes soluble and is easily removed during development. This process is called UV lithography. By sending UV light through a mask, we can transfer the pattern from the mask onto the photoresist [54]. Some photoresists called image reversed photoresists have a photoactive agent that makes the resist almost insoluble during development after baking at high temperature under UV exposure. Image reversed photoresist are used for lift-off process.

4.6 Processing steps

The processing of the device after MBE is done in three steps: RWG etching, opening and metallization.

4.6.1 RWG etching

Fig. 4.8 present a summary of the whole process. First, a SiO_2 layer is applied on the top of the device using PECVD. Then a photoresist is spread by spinning for UV lithography. After UV exposure through a lithography mask, some parts of the photoresist are dissolved and removed, leaving the SiO_2 layer exposed. The exposed SiO_2 is etched with RIE while the rest is protected by the photoresist. Finally, the photoresist is fully removed. Then, the etching of the exposed semiconductor is done with ICP while the rest is protected by the SiO_2 layer that acts as a mask. After the processing of the RWG, the remaining SiO_2 is removed by RIE etching.

4.6.2 Opening

When injecting current through the top of the device, all the flux of electrons must be directed toward the RWG. To achieve that, the semiconductor is covered with an isolating SiN layer with openings only on top of the RWG (as can be seen in Fig. 4.9). This is

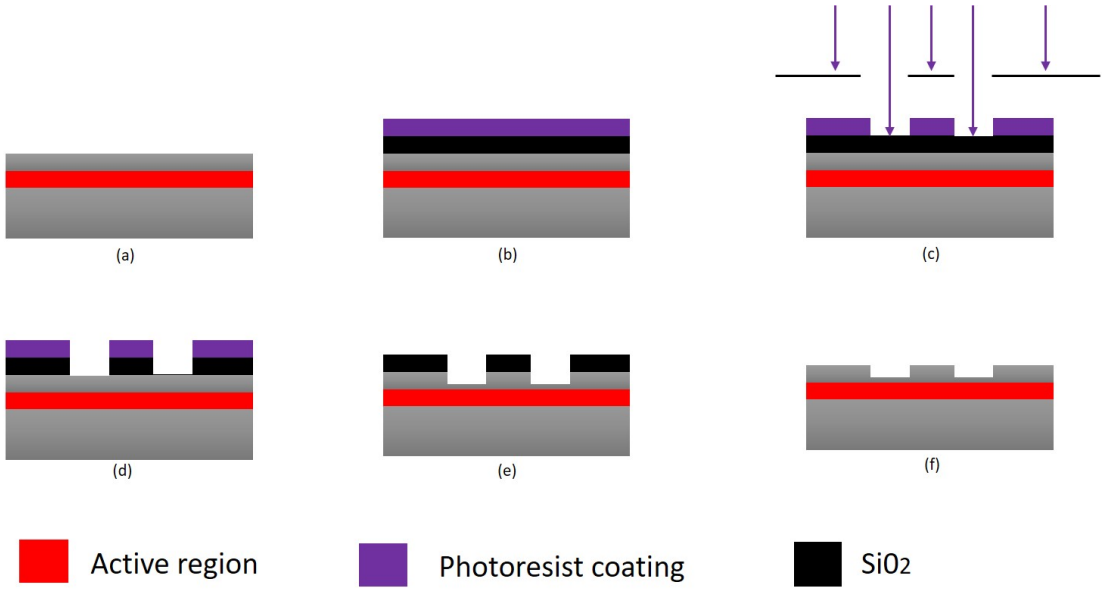

Figure 4.8. *Processing steps of RWG etching. (a) Unprocessed device. (b) growth of S_iO_2 layer (PECVD) and photoresist (spinning). (c) UV exposition through lithography mask. The exposed photoresist is dissolved and removed. (d) Etching of S_iO_2 unprotected by photoresist (RIE). (e) Photoresist removed. Etching of p layer unprotected by S_iO_2 (ICP). (f) S_iO_2 remove (wet etching).*

done in the same way as the RWG processing. SiN layer is grown using PECVD. Then the photoresist is spread on the surface and dissolved after UV exposure. The exposed SiN layer on top of the ridge waveguide is then etched, leaving an opening that let pass current from the metallic layer to the semiconductor part of the device.

4.6.3 Metallization

Metallization is a process that covers the top and bottom of the device with a conductive metal to allow the injection of current (see Fig. 4.10). As all the devices of a batch are built on a same bar, it is important to not connect adjacent RWG with metallic layers as it would hinder the dicing process. The process used during metallization is called lift-off process [55]. The photoresist used contains a special agent that is activated at high temperatures if the photoresist is also exposed to UV light. The area where the agent was activated becomes almost insoluble during development and is no longer light sensitive. On the other hand, the unexposed areas still behave like a normal positive photoresist [56]. This is called image reversal photoresist. The image reversed photoresist is put below the layer we want to remove. First, the photoresist is spread. Then by UV exposure through a mask, we image reverse the photoresist on the areas where we don't want metals. The unreversed photoresist is removed and the metallic layer is then grown using E-beam evaporation over the whole surface. Finally, the image reversed photoresist is removed and the metallic layer grown on top of it with it. We end up with a metallic layer

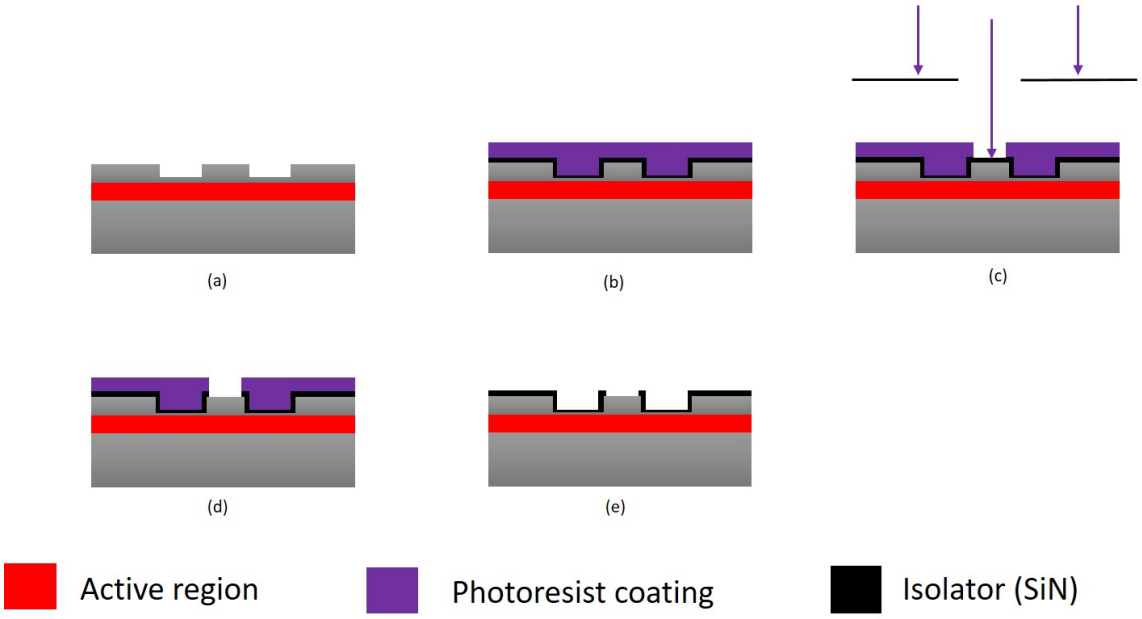

Figure 4.9. *Processing steps of opening. (a) Unisolated device. (b) growth of S_iN layer (PECVD) and photoresist (spinning). (c) UV exposition through lithography mask. Exposed photoresist is dissolved and removed. (d) Etching of S_iN unprotected by photoresist (RIE). (e) Photoresist removed. Top of the device isolated except the top of the RWG which is opened. Only the current injected through the top of the RWG contributes to the pumping.*

only around the RWG as it is there that we want to inject current.

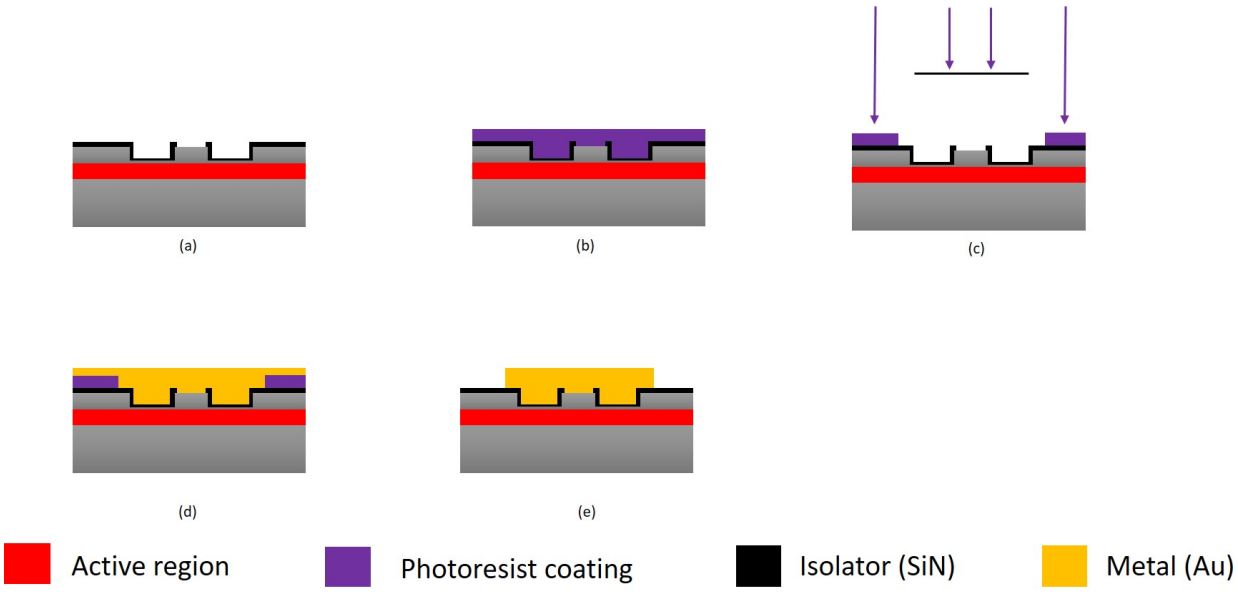

Figure 4.10. *Processing steps of metallization. (a) Unmetallized device. (b) spreading of negative photoresist (spinning). (c) UV exposition through lithography mask. The exposed photoresist is image reversed. Unexposed photoresist is removed. (d) Growth of metallic layer (E-beam evaporation). (e) Image reversed photoresist removed with the metallic layers on top of it. RWG of devices from the same batch are then isolated from each other.*

4.7 Last steps

4.7.1 Thinning

The wafer thickness play a major role in the diffusion of the temperature from the active region to the submount and for the electric conduction of the device. A low thickness has better electrical and thermal performance. But it also has a very low mechanical resistance. Devices with a wafer thinner than several hundreds of μm would probably break during the handling. To have the best performance, we can reduce the wafer width by thinning. The thinning reduce the thickness of the wafer from several hundreds of micrometer to only 100-150 um.

4.7.2 Dicing

Every device of a batch are built on the same bar. They must be separated before further processing. A thin scratch is made on the junction between two different LD. Then a strain is applied to break the junction along the scratch, effectively separating the two devices.

4.7.3 Mounting

Since the LDs are too small to be easily handled, they are fixed to a submount made of aluminum nitrid (AIN). In addition to improving the handling, the submount is also used to dissipate the thermal energy produced by the active region which increases the performance of the LD. The fixation is made with an industrial electrically conductive glue EPO-TEK MED-H20E. The glue is a thermosetting resin that becomes hard after being heated.

4.7.4 Wiring

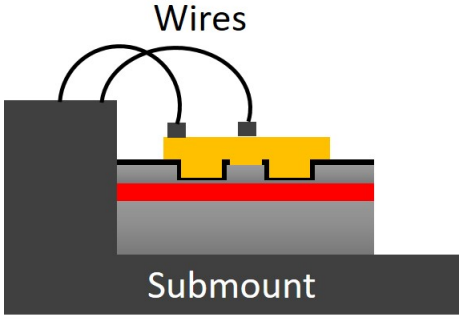

Figure 4.11. *Processed device*

The submount is used as a point of current injection into the device. To connect the top part with the submount, we use gold wires. The tip of the gold wire is melted with an

electrical arc and then gently pressed against the top of the LD. The other tip is fixed to the submount. The wired device is shown in Fig. 4.11.

5. RESULTS

5.1 Introduction

In this chapter, we are presenting the methods used to characterize the devices studied in this thesis and their results. SLEDs and MLLDs were characterized by measuring their optical power and extracting from the resulting I-P-V characteristic the threshold current, peak power and saturation current. We also did far field (FF) and spectral measurements.

5.2 Devices studied in the analysis

This section presents the devices studied in this chapter. The studied devices include: (i) 3 long shallow MLLDs emitting around 2 μm wavelength, (ii) 3 mm long deeply etched (DE) MLLDs emitting around 2 μm wavelength and (iii) 3 mm long SLEDs emitting around 2 μm and 2.6 μm wavelength. The design parameters of MLLDs and SLEDs are listed in tables 5.1 and 5.2 respectively:

Parameter	Value
Total length (L)	3000 μm
Length of gain section (L_{gain})	2650 μm
Length of saturable absorber (L_{SA})	300 μm
Length of isolation section (L_{iso})	50 μm
RWG width (w)	3 μm
RWG depth (d_{RWG})	1.5 μm

Table 5.1. *MLLD design parameters*

The epitaxial structure and the theory of those devices were discussed in the previous chapters. DE MLLDs have the same parameters as shallow MLLDs at the only difference that their RWG height is equal to 4 μm (instead of 1.5μm) in the isolation section.

Parameter	Value
Total length of the device (L)	3000 μm
Length of straight RWG ($L_{straight}$)	1500 μm
Length of bent RWG (L_{bent})	1500 μm
tilt angle (α)	7.5°
RWG width (w)	5 μm
Reflectivity of back facet (R1)	> 92 $\%$
Reflectivity of front facet (R2)	< 0.5$\%$

Table 5.2. *SLED design parameter*

5.3 Characterization methods

This section summarise the experimental setups used for the characterization of the devices. To make sure that all the measurements were done at the same temperature, The devices were thermoelectrically cooled at room temperature (20℃) by a temperature electronic controller (TEC).

5.3.1 Optical power measurement

I-P-V (current, optical power and voltage) measurement determines the device's light output power and the voltage through the gain section as a function of the injection current. The device is driven with a range of currents and the output power and voltage are measured for each current point. Many useful parameters can be derived from the I-P curve. This includes threshold current and saturation power. Fig. 5.1 shows an ideal I-P-V characteristic.

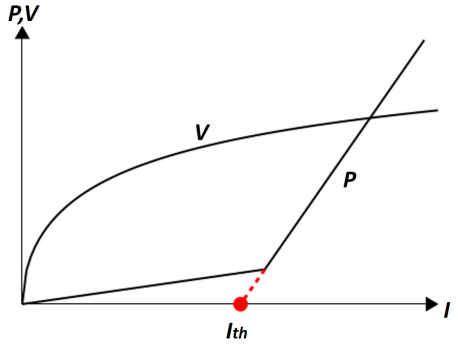

Figure 5.1. *Ideal I-P-V characteristic. P is the optical power measured and V is the positive voltage through the gain section induced by the injected current I. The threshold current Ith is defined to be the intersection between the extension of the I-P curve above threshold and the current axis.*

The setup for measuring optical power under pulsed operation is presented in Fig. 5.2.

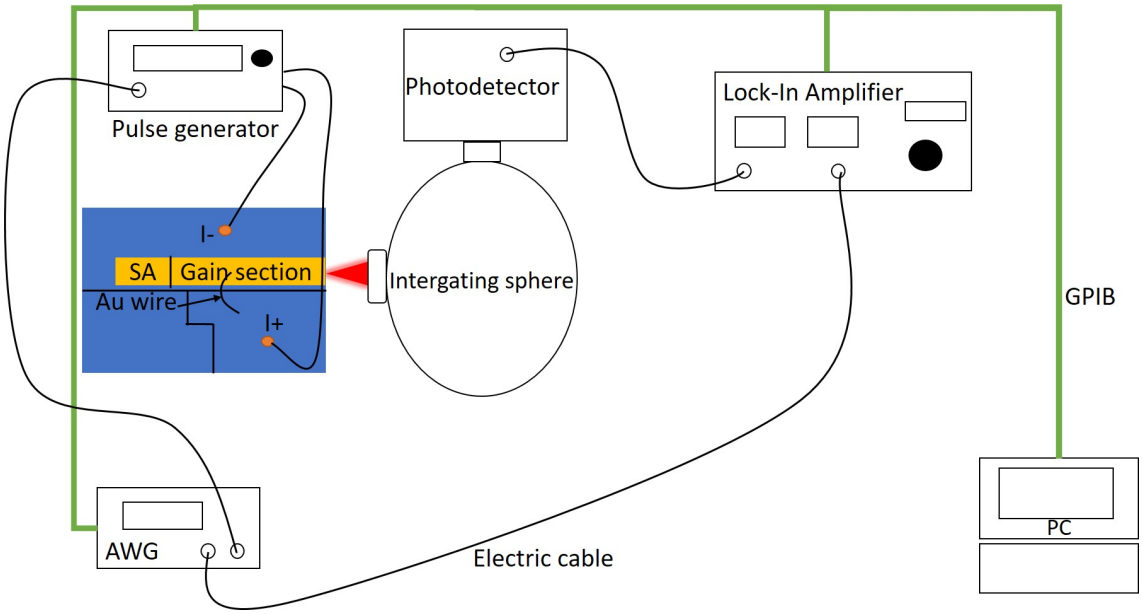

Figure 5.2. *Setup for measuring optical power under pulsed operation*

The light from the device is sent in an integrating sphere and collected by a photodetector. The integrating sphere is a hollow sphere with its surface covered with gold. Any light sent inside is reflected by the golden surface until it exits from the other port where the detector is placed. The integrating sphere is used to avoid variation of the detected power depending on the beam shape of the device. The photodetector can be changed in order to match the emission wavelength. A PVI-4TE-4 VIGO photodetector was used to detect light with wavelength between 2.5 and 3 μm and a PDA10D2 Thorlabs photodetector for wavelengths around 2 μm. The injection of pump current is done with a 2604B sourcemeter (Keithley) for CW operation and with a Laser Diode Driver (DEI) PCX-7410 combined with a 33220A Arbitrary wave form generator (AWG) (Agilent) for pulsed operation. The AWG is used to control the pulse length τ_p, repetition rate ν_p and duty cycle (DC) of the injected current. Before the measurements, the setup was calibrated to take into account the losses induced by the integrating sphere and the wavelength dependant photovoltaic response of the photodetector.

5.3.2 Far field beam profile

Measuring the far field (FF) beam profile of a device as a function of the output angle gives us precious hints on the stability of the device. It is desired for better coupling with optical fibers to have a Gaussian beam shape with an evenly proportioned fast and slow axis. Furthermore, a change in the beam shape at higher current could indicate an instability of the mode, either because of low confinement in the active region or because of the generation of new propagating modes. The setup for FF measurement is shown in Fig.

5.3.

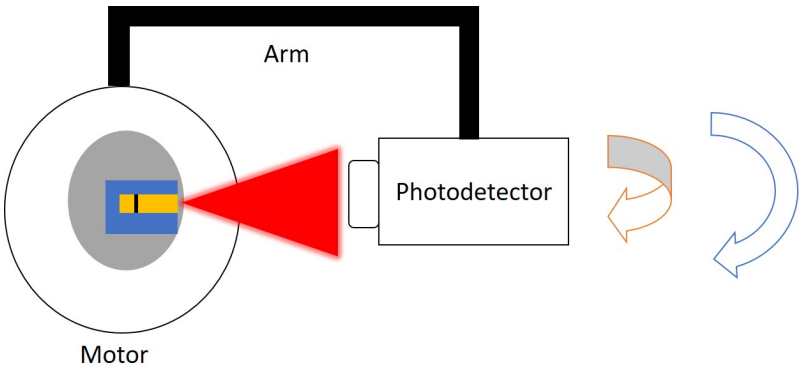

Figure 5.3. *Setup to measure the FF. The arm is able to move horizontally and vertically.*

The photodetector is fixed at one end of a mechanical arm. The arm is connected to a motor that allows the detector to move both vertically and horizontally. A scan is performed to measure the optical intensity of the output light as a function of the output angle along both fast and slow axis. After measuring the FF of the device, the full width at half maximum (FWHM) of the beam profile can be extracted.

5.3.3 Spectral measurement

The spectral measurement is done by coupling the output light to a bare single mode fiber. The optical fiber guide the light into an optical spectrum analyzer (OSA). The spectral measurement is done with an AQ6375 Yokogawa OSA. A schematic of the setup is shown in Fig. 5.4.

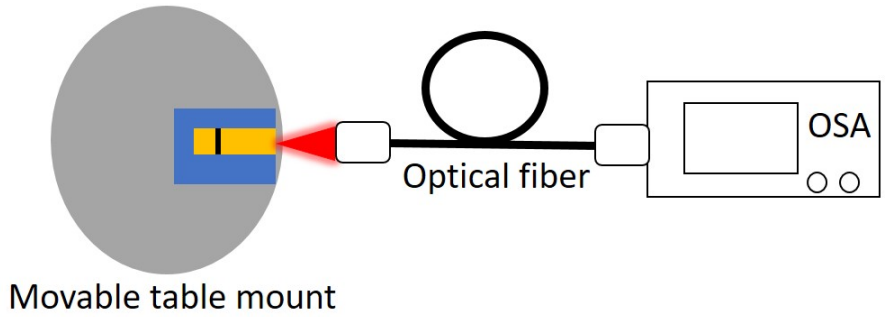

Figure 5.4. *Setup for spectral measurement*

5.4 Characterization of 2μm wavelength mode-locked laser diode

The effect of reverse bias applied on the SA section of a MLLD over its performance was investigated. Fig. 5.5(a) shows the evolution of the output power under CW operation as a function of the reverse bias applied on the SA. The mount was kept at room temperature with a TEC. As we can see, applying a reverse voltage to the SA increases its absorbance,

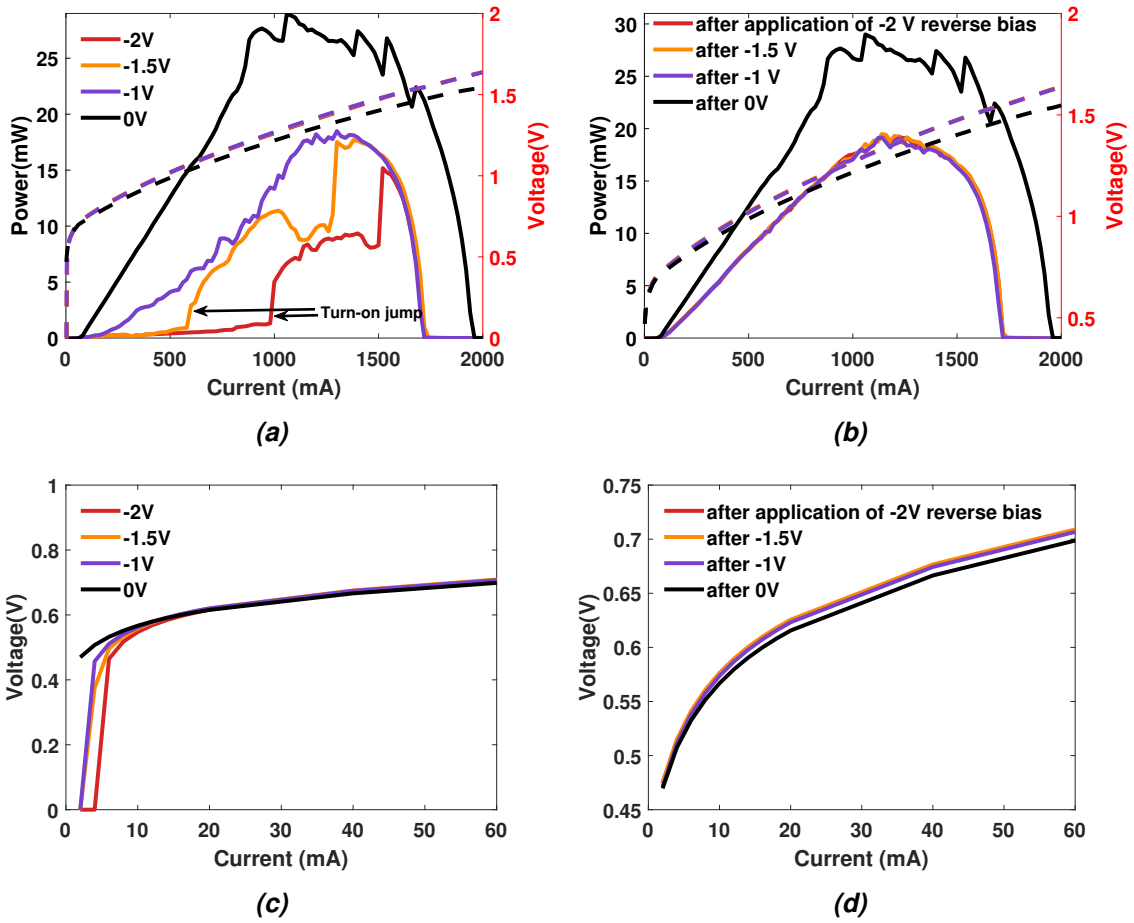

Figure 5.5. *Optical power measurement for 3 mm long shallow MLLD at room temperature under CW operation. (a) and (c) are respectively the I-P-V and the I-V characteristic of the device as a function of the reverse bias applied to the saturable absorber. (b) and (d) are respectively the I-P-V and the I-V characteristic before and after applying the reverse bias. The I-V characteristics are also plotted in (a) and (b) (dashed line)*

resulting in a reduction of the optical power under high reverse bias. The saturated power is reduced from 29mW to 15mW when the reverse bias is increased from 0V to -2V. The threshold current also increases consistently with increasing reverse bias, owing to the stronger absorption [4]. The decrease in power with increased reverse bias is due to electroabsorption [57]. When the SA is saturated, all the energy states of the conduction band are occupied. Applying a reverse bias sweep the electrons out of the conduction band, increasing the number of unoccupied states. This increases the absorption rate of electrons from the valence band and thus, the absorption coefficient of the SA [58].

The I-P curve exhibits a turn-on jump at lasing threshold under high reverse bias (particularly visible under -1.5 and -2V reverse bias). Such jump is common in devices with a SA and is attributed to a reduction of the SA absorbance due to a rapid increase of the carrier density in the SA QW region. As the lasing operation start, the photon density increases quickly. The electric field generated by the reverse bias is not strong enough to sweep the

carriers out of the SA QW region immediately. Thus, the carrier density in the QW region increases, reducing the absorption of the SA and resulting in an output power jump [59].

As shown in Fig. 5.5(b), applying a reverse bias of -1V and above created catastrophic degradation in the laser material. Such degradation was attributed to the heat generated by free carrier absorption in the top cladding of the isolation section. Due to carrier leakage between the gain section and the SA, the carrier density is very high in the top cladding of the isolation section. This results in a high rate of free-carrier absorption, generating heat. In case of high power devices, like the ones we are studying, the generated heat can be strong enough to create defects due to local melting in the device, permanently reducing its output power [60]. On the other hand, low power and deeply etched devices (that don't have current leakage) can withstand strong reverse bias without damage, as can be seen in Fig. 5.8(b).

The voltage through the gain section was measured and plotted as a function of the injected current. The results are shown in Fig. 5.5.(c) and (d). From Fig. 5.5.(c), we can observe a shift of the I-V characteristic of the device with the reverse bias. This shift can be explained by current leakage through the isolation section. As the reverse bias applied to the SA increases, the voltage in the gain section drops due to poor electrical isolation between the two, thus increasing the current required to maintain a given forward voltage. In Fig. 5.5.(d), the voltage was measured when no reverse was applied. Unlike Fig. 5.5.(c), there were no changes in the I-V characteristic, demonstrating that the shift of the I-V characteristic is due to current leakage.

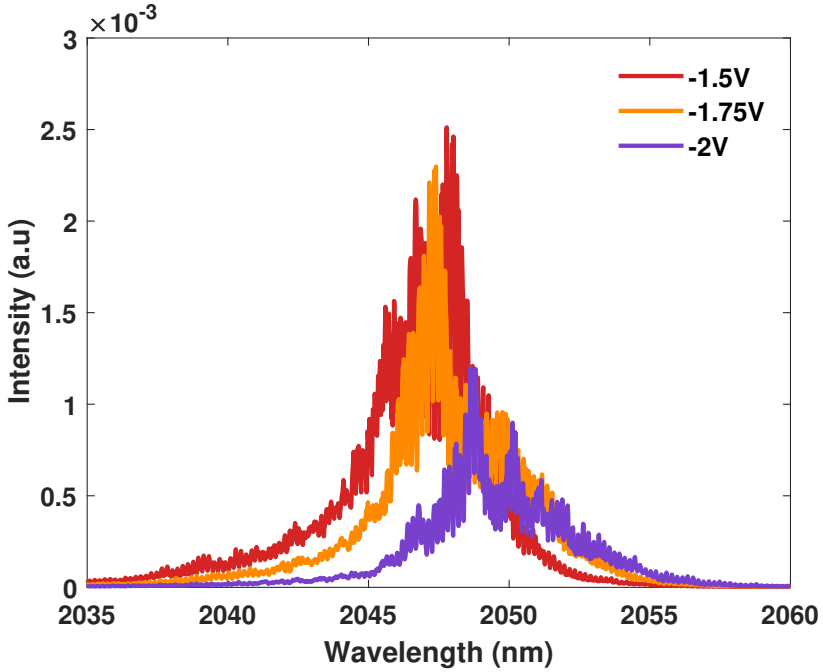

Figure 5.6. *Spectrum of shallow MLLD at different injected reverse voltage. The device is under CW operation with 1A pump current*

The spectrum of emission of our device was analyzed to check if a mode locking behavior was observable. The reverse bias was increased from -1.5 to -2V. The measured spectrum, shown in Fig. 5.6, has a FWHM of around 3 nm and more than 20 longitudinal modes when the reverse bias is increased from 1.5V to -2V. Such spectrum shape is typical of mode-locked devices. This spectrum, as well as the turn-on jump in Fig. 5.5(a), indicate mode-locking at these operation conditions.

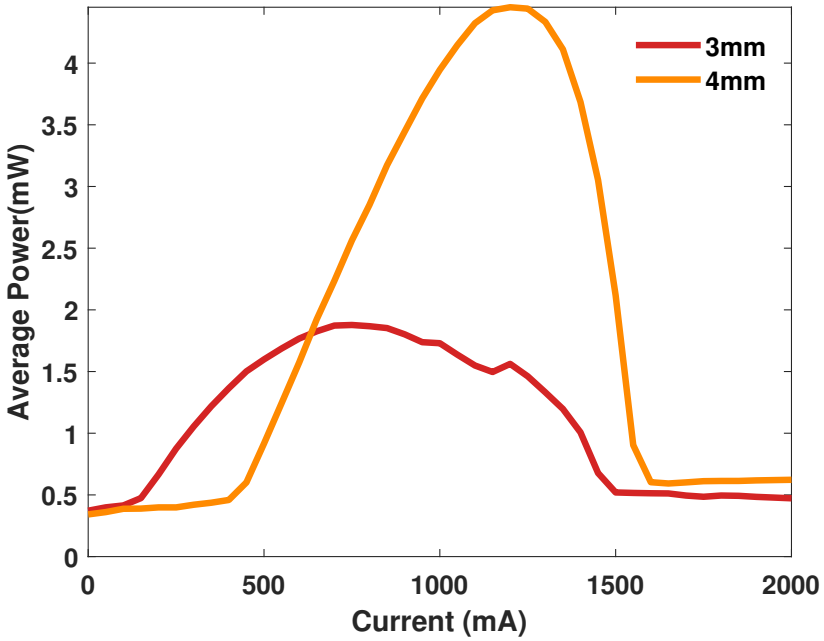

Figure 5.7. *Optical power of shallow MLLD at different cavity lengths*

The effect of the size of a device over its performance was investigated. The length of the SA was kept at 10% of the total length of the FP cavity for both devices. Both share the same epitaxial structure. The I-P characteristic of 3mm long and 4mm long devices were plotted and are shown in Fig. 5.7. As can be seen, the saturation power is almost multiplied by 2, going from 2mW to 4.5mW for 3mm long and 4mm long devices respectively. This difference in optical power can be explained by the single pass gain that increases exponentially with the increase in cavity length. The threshold current increases from 41mA for the 3mm long device to 376mA for the 4mm long device. This is due to the higher number of charge carriers in the gain section for longer devices, thus requiring a stronger current to achieve an inversion of population. The saturation current is also increased for longer devices as the higher active region volume requires more current to reach the temperature of saturation. Therefore, a longer device has a stronger optical power due to increased feedback gain but also requires more injection current in order to reach the lasing threshold.

The I-V characteristic of the DE MLLD under CW operation at room temperature is shown in Fig. 5.8(a). The reverse current applied to the SA was varied from 0 to -5V. As can be

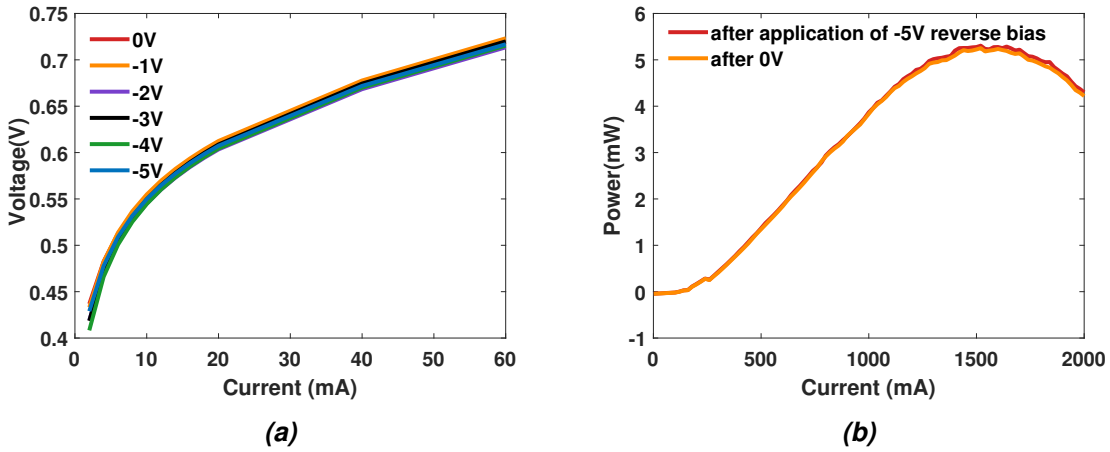

Figure 5.8. *(a):I-V curve of DE MLLD as a function of the reverse bias applied to the saturable absorber. (b): I-P curve of DE MLLD before and after application of a reverse bias*

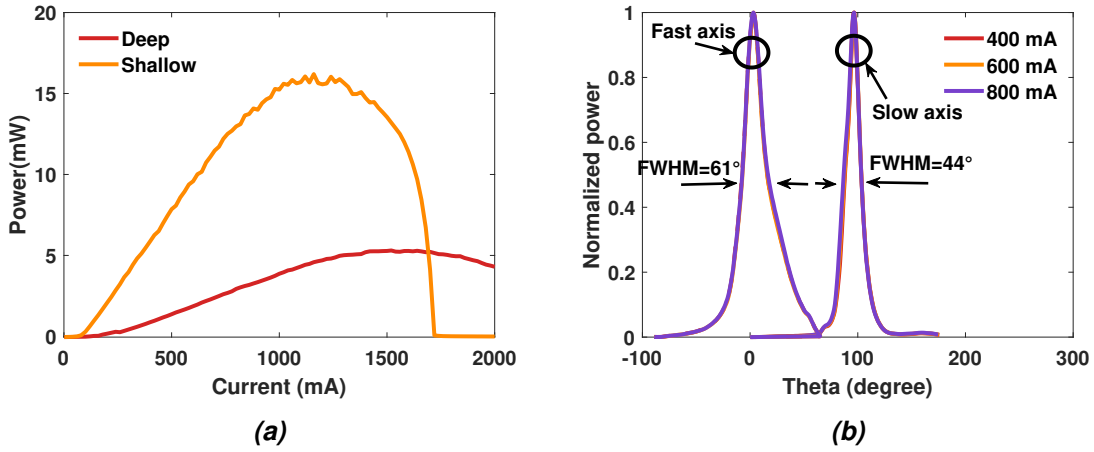

Figure 5.9. *(a):I-P characteristic of shallow MLLD compared to DE MLLD. (b): Far field of DE MLLD at different injected current*

seen, the I-V characteristic of the device remains unchanged by the reverse bias. We can deduce that the deep etching effectively increased the resistance of the isolation section and prevented a current leakage between the gain section and the SA. Fig. 5.8(b) shows the I-P characteristic of the DE MLLD before and after application of the reverse bias. We can see that no catastrophic degradation occurred, due to the low power of the device (5mW) and the reduced current leakage.

In Fig. 5.9(a), the I-P characteristic of shallow MLLD and DE MLLD were compared. Both have the same epitaxial structure and length of 3mm. A CW injection current was used for each and the temperature was stabilized at room temperature by TEC. Fig. 5.9(a) shows that deep etching reduces the output power of the device from 15mW to 5mW. This was attributed to the increased losses in the isolation section. The FF of DE MLLD was investigated to check that the deepening of the RWG in the isolation section didn't affect

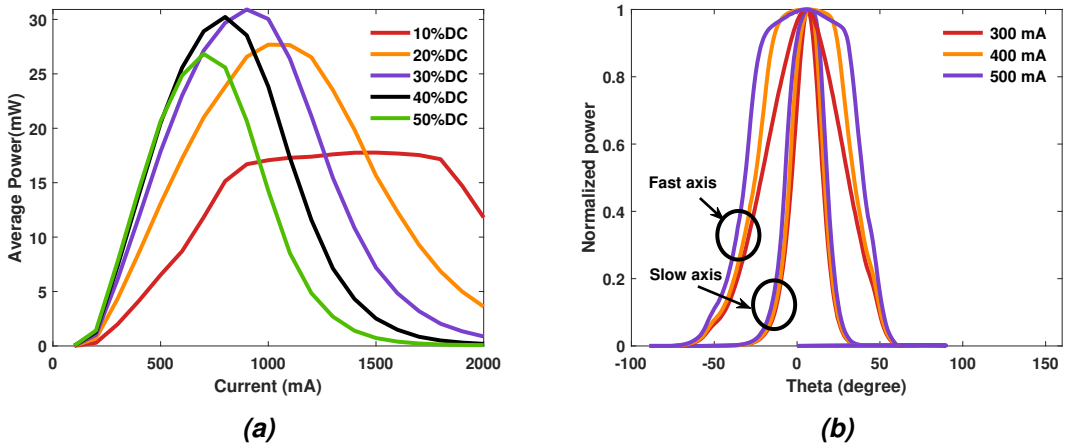

Figure 5.10. *(a):Optical power of SLED at different injected DC. (b): Far field of 2.6μm wavelength SLED device at different injected current*

the stability of the device. The FF plot is shown in Fig. 5.9(b) and shows that the shape and the FWHM of the FF stay unchanged for each different current value. Therefore, the device remains stable despite the deep etching. We can observe that the slow axis is shifted compared to the fast axis centered at 0°. This is only due to a misalignment of the photodetector during the measurement.

5.5 Characterization of superluminescent diode

5.5.1 2.6μm wavelength emitting SLED

Fig. 5.10(a) shows the optical output of a SLED device as a function of the duty-cycle (DC) of the injected pulsed pump current. The repetition rate of the injection current was constant at 100KHz for every different DC. We can observe that the saturation current decreases consistently from 1400 at 10$\%$ DC to 670 mA at 50$\%$ DC. This can be explained by the increase of self-heating due to Joule effect for increased pulse length. Due to that, the active region reaches a critical temperature at lower current, effectively reducing the saturation current. We can see from Fig 5.10(a) that the saturation power of the device is increasing with the DC until 30$\%$ DC before decreasing. The reason for this is the increase of current density at higher DC that also increases the output power of the device. However, past 30$\%$ DC, the losses due to self heating exceed the gain due to high carrier density, reducing the optical power of the device.

Presented in Fig. 5.10(b) is the FF of the 2.6μm wavelength SLED. As we can see, the output beam of the device presents some instability, particularly along the fast axis. New modes appear at higher injection current and widen the beam profile along the fast axis from 52° at 300mA to 69° at 500mA. Such instability is a crucial issue as it hinders the coupling of the beam with optical fibers and single mode waveguides.

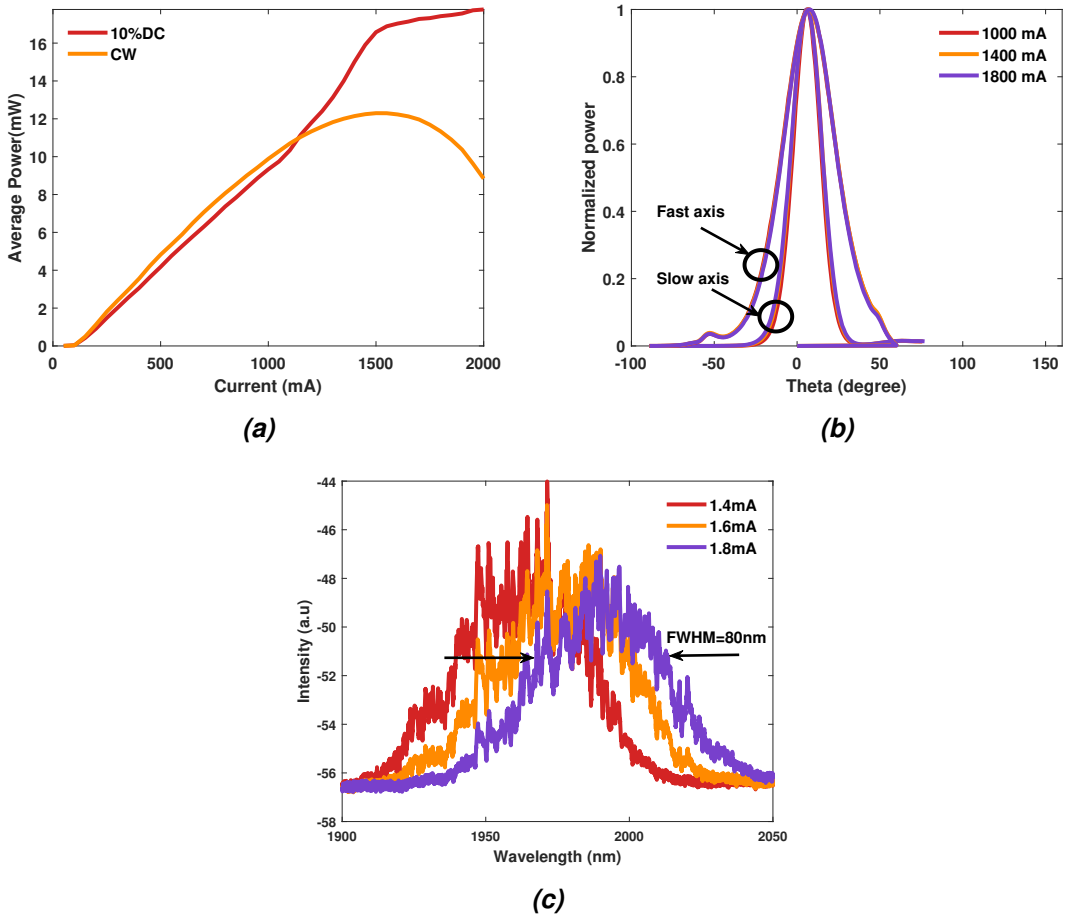

Figure 5.11. *(a):Optical power of 2 μm SLED as a function of the type of injected current. (b): Far field of 2 μm wavelength SLED device at different injected current. (c): Spectrum of 2 μm wavelength SLED device at different injected current*

5.5.2 2 μm wavelength emitting SLED

The output power of the device was measured as a function of the injection current for a pulsed pump at 10% duty cycle (DC) and for a CW pump. The 10% DC pump has a pulse width of 1μm and a repetition rate of 100KHz. The results are reported in Fig. 5.11(a)

As shown, the device exhibits power saturation at a saturation power of 12.3mW under CW operation. The power saturation is attributed to self-heating in the active region caused by Joule effect. Using a CW pump increases the self-heating compared to a pulsed pump. Thus, the CW operation limits the saturation power of the device to 12.3mW while an optical power up to 17.8mW was achieved under a 10% DC operation and no power roll-over was observed. There is a slight inconsistency as the CW pump did not increase the threshold current (which is exponentially dependant on the temperature in the active region). This might be due to unknown damage to the device. The non linearity of the output power at high current for pulsed operation could also be due to some unknown damage.

Fig. 5.11(b) demonstrates the quality of the beam shape and the stability of the mode confinement in the device. The slow and fast axis remains stable no matter the current used with the slow axis at 37° and the fast axis at 67°. Unlike 2.6μm devices, the shape of the FF is not affected by the current and remain Gaussian. There are no new modes appearing on the sides of the main peak and the FWHM stays constant for both axis. Those measurements show that 2μm devices have a good beam profile and good stability along the fast and slow axis.

Finally, the spectrum of the SLED device was measured to check that it has a proper SLED operation and not a lasing operation. The device is expected to have a wide spectrum due to ASE behavior. Fig. 5.11(c) shows the measured spectrum at different current values under CW operation. We can see that increasing the current shift the peak wavelength toward higher values. The peak wavelength is equal to 1964nm for 1.4mA injected current and equal to 1990mA for 1.8mA injected current which corresponds to a wavelength shift of 26nm. This shift is due to the increase of temperature in the active region that shrinks the bandgap between conduction and valence bands and so reduces the energy of the emitted photons. It is also due, in a lesser way, to the increased carrier concentration at high injection current that induces bandgap shrinkage and thus increases the emission wavelength (many-body effect) [13, 22]. The FWHM of the spectrum was measured equal to 80nm for every current with more than 20 longitudinal modes. This spectrum indicates superluminescent operation. The optical feedback was adequately reduced to prevent lasing operation. Furthermore, the peak wavelength is close to 2μm, which corresponds to our expectations.

6. CONCLUSION

In this thesis, a set of GaSb-based mid-IR light emitting devices, including passive mode-locked laser diodes (MLLD) and superluminescent light emitting diodes, were successfully developed and characterized. Two epitaxial structures with an InGaSb and an InGaAsSb active layer, emitting at 2 μm and 2.6 μm wavelength respectively, were designed. The devices were grown on a GaSb substrate by MBE and were processed in to cleanroom. SLEDs device emitting at 2 μm and 2.6 μm wavelength were developed and characterized.

Different straight waveguide lengths of MLLD were characterized. Two different waveguide designs for 2 μm wavelength MLLD devices with variable etching depth were developed to get increased isolation between the gain section and the saturable absorber (SA). Their performance was compared. Deeply etched (DE) MLLD were found to have higher electrical resistance in the isolation section than shallow MLLD. Power up to 5mW was achieved with DE MLLD compared to a saturation power of 15mW for shallow MLLD. The optical power of MLLD was seen reduced when applying an increasing reverse bias due to electroabsorption. A turn-on jump of the I-P characteristic was observed which could be an indication of mode-locking operation. It was shown that the deep etching didn't affect the mode confinement stability of the device.

For SLEDs, a reduction of optical power under high pulse length of the pump current was observed. The reduction of power was attributed to increased self-heating. An increase of the emission wavelength was observed for increasing pump current due to heating and many-body effect. Power as high as 31mW was achieved from 2.6 μm SLED with a pulsed pump current of 30$\%$ DC. 2.6 μm SLEDs were found to have unstable mode confinement and beam profile.

Future development includes the characterization of MLLD by measuring RF spectrum to confirm the pulsed operation. Improved electrical isolation is needed between gain and isolation section. In terms of SLED, the improvement comes from the reduction of Auger recombination through new epi designs and the extension of wavelength towards 3µm.

REFERENCES

[1] Kawanishi, S. Ultrahigh-speed optical time-division-multiplexed transmission technology based on optical signal processing. *IEEE Journal of Quantum Electronics* 34.11 (1998), pp. 2064–2079.

[2] Picqué, N. and Hänsch, T. W. Frequency comb spectroscopy. *Nature Photonics* 13.3 (2019), pp. 146–157.

[3] Zia, N., Viheriälä, J., Koivusalo, E. and Guina, M. High-power single mode GaSb-based 2 μ m superluminescent diode with double-pass gain. *Applied Physics Letters* 115.23 (2019), p. 231106.

[4] Li, X. Design, fabrication, and investigation of 2 μm GaSb-based diode lasers. ().

[5] Joullié, A., Christol, P., Baranov, A. N. and Vicet, A. Mid-Infrared 2—5 μm Heterojunction Laser Diodes. *Solid-State Mid-Infrared Laser Sources* (2003), pp. 1–61.

[6] Svelto, O. and Hanna, D. C. *Principles of lasers*. Vol. 4. Springer, 1998.

[7] Li, X., Wang, H., Qiao, Z., Guo, X., Wang, W., Sia, J. X. B., Ng, G. I., Zhang, Y., Niu, Z., Tong, C. et al. High temperature characteristics of a 2 μ m InGaSb/AlGaAsSb passively mode-locked quantum well laser. *Applied Physics Letters* 114.22 (2019), p. 221104.

[8] Kafar, A., Stanczyk, S., Schiavon, D., Suski, T. and Perlin, P. review on optimization and current status of (Al, In) GaN superluminescent diodes. *ECS Journal of Solid State Science and Technology* 9.1 (2019), p. 015010.

[9] Kafar, A., Stańczyk, S., Wiśniewski, P., Oto, T., Makarowa, I., Targowski, G., Suski, T. and Perlin, P. Design and optimization of InGaN superluminescent diodes. *physica status solidi (a)* 212.5 (2015), pp. 997–1004.

[10] Freeman, M., Champion, M. and Madhavan, S. Scanned laser pico-projectors: seeing the big picture (with a small device). *Optics and photonics news* 20.5 (2009), pp. 28–34.

[11] Singh, J. *Electronic and optoelectronic properties of semiconductor structures*. Cambridge University Press, 2007.

[12] Coldren, L. A., Corzine, S. W. and Mashanovitch, M. L. *Diode lasers and photonic integrated circuits*. Vol. 218. John Wiley & Sons, 2012.

[13] Piprek, J. *Semiconductor optoelectronic devices: introduction to physics and simulation*. Elsevier, 2013.

[14] Fojtik, A., Oswald, J., Kalal, M. and Duchon, J. Spectral properties of semiconductor quantum nanoparticles. *Frontiers of plasma physics and technology. Proceedings of an international conference*. 2008.

[15] Suhara, T. *Semiconductor laser fundamentals*. CRC press, 2004.

[16] Rosencher, E. and Vinter, B. *Optoelectronics*. Cambridge University Press, 2002.

[17] Connelly, M. J. *Semiconductor optical amplifiers*. Springer Science & Business Media, 2007.

[18] Andreev, A. D. and Donetsky, D. V. Analysis of temperature dependence of the threshold current in 2.3–2.6 μm InGaAsSb/AlGaAsSb quantum-well lasers. *Applied physics letters* 74.19 (1999), pp. 2743–2745.

[19] Sugimura, A. Band-to-band Auger effect in long wavelength multinary III-V alloy semiconductor lasers. *IEEE Journal of Quantum Electronics* 18.3 (1982), pp. 352–363.

[20] Dutta, N. and Nelson, R. The case for Auger recombination in In1- x Ga x As y P1- y. *Journal of Applied Physics* 53.1 (1982), pp. 74–92.

[21] Paschotta, R. Laser diodes. *Encyclopedia of Laser Physics and Technology* (2016).

[22] Agrawal, G. P. and Dutta, N. K. *Semiconductor lasers*. Springer Science & Business Media, 2013.

[23] Murakami, A., Kawashima, K. and Atsuki, K. Cavity resonance shift and bandwidth enhancement in semiconductor lasers with strong light injection. *IEEE journal of quantum electronics* 39.10 (2003), pp. 1196–1204.

[24] Olszewski, S. The de Broglie Waves and Joule-Lenz Law Applied in Examining the Electron Transitions in Small Quantum Systems. *Journal of Modern Physics* 10.2 (2019), pp. 176–194.

[25] Anthony, P. and Schumaker, N. Temperature dependence of the lasing threshold current of double heterostructure injection lasers due to drift current loss. *Journal of Applied Physics* 51.9 (1980), pp. 5038–5040.

[26] Shterengas, L., Belenky, G., Kim, J. and Martinelli, R. Design of high-power room-temperature continuous-wave GaSb-based type-I quantum-well lasers with λ> 2.5 μm. *Semiconductor science and technology* 19.5 (2004), p. 655.

[27] Salhi, A., Chi, P. C., Alharbi, A., Petrich, G. S., Al-Muhanna, A. and Kolodziejski, L. A. Temperature Dependence of Optical Gain and Loss in 2-μm InP Lasers. *IEEE Photonics Technology Letters* 23.20 (2011), pp. 1523–1525.

[28] Streetman, B. G., Banerjee, S. et al. *Solid state electronic devices*. Vol. 10. Pearson/Prentice Hall Upper Saddle River, NJ, 2006.

[29] Javaloyes, J. and Balle, S. Mode-locking in semiconductor Fabry-Perot lasers. *IEEE Journal of Quantum Electronics* 46.7 (2010), pp. 1023–1030.

[30] Becker, S., Scheuermann, J., Weih, R., Rößner, K., Kistner, C., Koeth, J., Hillbrand, J., Schwarz, B. and Kamp, M. Picosecond pulses from a monolithic GaSb-based passive mode-locked laser. *Applied Physics Letters* 116.2 (2020), p. 022102.

[31] Malins, D., Gomez-Iglesias, A., White, S., Sibbett, W., Miller, A. and Rafailov, E. Ultrafast electroabsorption dynamics in an InAs quantum dot saturable absorber at 1.3 μ m. *Applied Physics Letters* 89.17 (2006), p. 171111.

[32] Kunimatsu, D., Arahira, S., Kato, Y. and Ogawa, Y. Passively mode-locked laser diodes with bandgap-wavelength detuned saturable absorbers. *IEEE Photonics Technology Letters* 11.11 (1999), pp. 1363–1365.

[33] Alphonse, G. A., Gilbert, D. B., Harvey, M. and Ettenberg, M. High-power superluminescent diodes. *IEEE Journal of Quantum Electronics* 24.12 (1988), pp. 2454–2457.

[34] Kopp, F., Lermer, T., Eichler, C. and Strauss, U. Cyan superluminescent light-emitting diode based on InGaN quantum wells. *Applied Physics Express* 5.8 (2012), p. 082105.

[35] Huang, Y.-Z., Pan, Z. and Wu, R.-H. Analysis of the optical confinement factor in semiconductor lasers. *Journal of applied physics* 79.8 (1996), pp. 3827–3830.

[36] Botez, D. InGaAsP/InP double-heterostructure lasers: Simple expressions for wave confinement, beamwidth, and threshold current over wide ranges in wavelength (1.1-1.65 μm). *IEEE Journal of Quantum Electronics* 17.2 (1981), pp. 178–186.

[37] Tsang, W. The effects of lateral current spreading, carrier out-diffusion, and optical mode losses on the threshold current density of GaAs-AlχGa1- χAs stripe-geometry DH lasers. *Journal of Applied Physics* 49.3 (1978), pp. 1031–1044.

[38] Merghem, K., Teissier, R., Aubin, G., Monakhov, A., Ramdane, A. and Baranov, A. Passive mode locking of a GaSb-based quantum well diode laser emitting at 2.1 μ m. *Applied Physics Letters* 107.11 (2015), p. 111109.

[39] Olsson, N. A. Lightwave systems with optical amplifiers. *Journal of Lightwave Technology* 7.7 (1989), pp. 1071–1082.

[40] Kafar, A., Stańczyk, S., Grzanka, S., Czernecki, R., Leszczyński, M., Suski, T. and Perlin, P. Cavity suppression in nitride based superluminescent diodes. *Journal of Applied Physics* 111.8 (2012), p. 083106.

[41] Kopp, F., Eichler, C., Lell, A., Tautz, S., Ristić, J., Stojetz, B., Höß, C., Weig, T., Schwarz, U. T. and Strauss, U. Blue superluminescent light-emitting diodes with output power above 100 mW for picoprojection. *Japanese Journal of Applied Physics* 52.8S (2013), 08JH07.

[42] Sweeney, S. J., Eales, T. D. and Adams, A. R. The impact of strained layers on current and emerging semiconductor laser systems. *Journal of Applied Physics* 125.8 (2019), p. 082538.

[43] Turner, G., Choi, H. and Manfra, M. Ultralow-threshold (50 A/cm 2) strained single-quantum-well GaInAsSb/AlGaAsSb lasers emitting at 2.05 μm. *Applied physics letters* 72.8 (1998), pp. 876–878.

[44] Leeson, N. Quantum Well Intermixed Two Section Superluminescent Diodes. PhD thesis. 2008.

[45] Vurgaftman, I., Meyer, J. á. and Ram-Mohan, L. á. Band parameters for III–V compound semiconductors and their alloys. *Journal of applied physics* 89.11 (2001), pp. 5815–5875.

[46] Corzine, S. W., Yan, R.-H. and Coldren, L. A. Optical gain in III-V bulk and quantum well semiconductors. *Quantum well lasers(A 95-14956 02-36), San Diego, CA, Academic Press, Inc., 1993,* (1993), pp. 17–96.

[47] Saleh, B. E. and Teich, M. C. *Fundamentals of photonics*. john Wiley & sons, 2019.

[48] Simanowski, S., Walther, M., Schmitz, J., Kiefer, R., Herres, N., Fuchs, F., Maier, M., Mermelstein, C., Wagner, J. and Weimann, G. Arsenic incorporation in molecular beam epitaxy (MBE) grown (AlGaIn)(AsSb) layers for 2.0–2.5 μm laser structures on GaSb substrates. *Journal of crystal growth* 201 (1999), pp. 849–853.

[49] Newell, T., Wu, X., Gray, A., Dorato, S., Lee, H. and Lester, L. The effect of increased valence band offset on the operation of 2 μm GaInAsSb-AlGaAsSb lasers. *IEEE Photonics Technology Letters* 11.1 (1999), pp. 30–32.

[50] Garbuzov, D. Z., Lee, H., York, P. K., Menna, R. J., Martinelli, R. U., DiMarco, L. A., Narayan, S. Y., Capewell, D. R. and Connolly, J. C. AlGaAsSb/InGaAsSb/GaSb quantum well lasers with separate confinement heterostructures for 2-um operation. *Laser Diodes and Applications II*. Vol. 2682. International Society for Optics and Photonics. 1996, pp. 216–223.

[51] Henini, M. *Molecular beam epitaxy: from research to mass production*. Newnes, 2012.

[52] Baca, A. G. and Ashby, C. I. *Fabrication of GaAs devices*. 6. IET, 2005.

[53] Youtsey, C. and Adesida, I. Plasma processing of III-V materials. *Handbook of Advanced Plasma Processing Techniques*. Springer, 2000, pp. 459–505.

[54] Leinonen, P. *Techniques for semiconductor laser processing*. Tampere University of Technology, 2007.

[55] Van Zant, P. *Microchip fabrication*. McGraw-Hill Education, 2014.

[56] Clariant. AZ5214E Image reversal photoresist. ().

[57] Huang, X., Stintz, A., Li, H., Rice, A., Liu, G., Lester, L., Cheng, J. and Malloy, M. Bistable operation of a two-section 1.3/spl mu/m InAs quantum dot laser-absorption saturation and the quantum confined Stark effect. *IEEE journal of quantum electronics* 37.3 (2001), pp. 414–417.

[58] Thompson, M. G., Rae, A. R., Xia, M., Penty, R. V. and White, I. H. InGaAs quantum-dot mode-locked laser diodes. *IEEE Journal of Selected Topics in Quantum Electronics* 15.3 (2009), pp. 661–672.

[59] Li, X., Wang, H., Qiao, Z., Guo, X., Ng, G. I., Zhang, Y., Niu, Z., Tong, C. and Liu, C. Modal gain characteristics of a 2 μ m InGaSb/AlGaAsSb passively mode-locked quantum well laser. *Applied Physics Letters* 111.25 (2017), p. 251105.

[60] Henry, C., Petroff, P., Logan, R. and Merritt, F. Catastrophic damage of Al x Ga1-x As double-heterostructure laser material. *Journal of applied physics* 50.5 (1979), pp. 3721–3732.